

Interferometric Lensless Imaging: Rank-one Projections of Image Frequencies with Speckle Illuminations

Olivier Leblanc*, Mathias Hofer†, Siddharth Sivankutty‡, Hervé Rigneault†, and Laurent Jacques*

Abstract—Lensless illumination single-pixel imaging with a multi-core fiber (MCF) is a computational imaging technique that enables potential endoscopic observations of biological samples at cellular scale. In this work, we show that this technique is tantamount to collecting multiple symmetric rank-one projections (SROP) of an *interferometric* matrix—a matrix encoding the spectral content of the sample image. In this model, each SROP is induced by the complex *sketching* vector shaping the incident light wavefront with a spatial light modulator (SLM), while the projected interferometric matrix collects up to $O(Q^2)$ image frequencies for a Q -core MCF. While this scheme subsumes previous sensing modalities, such as raster scanning (RS) imaging with beamformed illumination, we demonstrate that collecting the measurements of M random SLM configurations—and thus acquiring M SROPs—allows us to estimate an image of interest if M and Q scale log-linearly with the image sparsity level. This demonstration is achieved both theoretically, with a specific restricted isometry analysis of the sensing scheme, and with extensive Monte Carlo experiments. On a practical side, we perform a single calibration of the sensing system robust to certain deviations to the theoretical model and independent of the *sketching* vectors used during the imaging phase. Experimental results made on an actual MCF system demonstrate the effectiveness of this imaging procedure on a benchmark image.

Keywords—lensless imaging, rank-one projections, interferometric matrix, inverse problem, computational imaging, single-pixel

I. INTRODUCTION

The advent of Computational Imaging (CI) can be traced back to the work of Ables [1] and Dicke [2] on coded aperture for x-ray and gamma ray imagers. Since then, an ever-growing number of solutions have been devised to relax the constraints imposed by more traditional optical architectures (when these exist). Cheaper, lighter, and enabling larger imaging field-of-view (FOV), Lensless Imaging (LI), a subfield of CI, is convenient for medical applications such as microscopy [3] and *in vivo* imaging [4] where the extreme miniaturization of the imaging probe (with a diameter $\leq 200 \mu\text{m}$) offers a minimally invasive route to image at depths unreachable in microscopy [5]. More recently, intensive research effort emerged for Lensless Endoscopy (LE) using multimode [6–8] or MultiCore Fibers (MCF) [9,10], paving the way for deep biological tissues [11] and brain imaging.

In CI applications, a mathematical model describes the observations as a function of the object to be imaged. Two efficiency requirements are considered; (i) the model, while physically reliable, must be computationally efficient to speed up the reconstruction algorithms; (ii) the acquisition method must minimize

the number of observations (also called *sample complexity*) needed to accurately estimate the object. In single-pixel MCF-LI, *Speckle Imaging* (SI) consists in randomly shaping the wavefront of the light input to the cores entering the MCF to illuminate the entire object with a randomly distributed intensity. The fraction of the light re-emitted (either at other wavelengths by fluorescence or by simple reflection) is integrated in a single-pixel sensor, playing the role of a complete projection of the speckle on the object. Compared to Raster Scanning (RS) the object with a translating focused (beamformed) spot [9], SI reduces the overall sample complexity needed to estimate a reliable image [12].

In this work, we improve the MCF-LI sensing model jointly on its reliability, computation and calibration. We achieve this by introducing light propagation physics in the forward model of MCF imaging, while keeping the low sample complexity enabled by SI. Inserting the physics yields a sensing model similar to radio-interferometry applications [13], where the interferences of the light emitted by the cores composing the MCF give specific access to the Fourier content of the object to be imaged. The sample complexity of the underlying model is analyzed both theoretically and experimentally.

A. Related works

In 2008, Duarte *et al.* introduced single-pixel imaging [14,15], a subfield of lensless imaging (LI) where each collected observation is equivalent to randomly modulating an image before integrating its intensity. They demonstrated that reliable image estimation is possible at low sampling rates compared to image resolution by using compressive sensing. More recently, this principle has been integrated into the use of an MCF for both remote illumination and image collection. This technique allows for both deep and large FOV imaging [9,12,16]. Subsequent works have shown that de-structured speckle-based illuminations can replace structured or beamformed illuminations effectively [12,17].

MCF-LI bears similarities with quadratic measurement models such as *phase retrieval* (PR) [18,19] whose sensing is often recast as SROPs of the *lifted* matrix $\mathbf{x}\mathbf{x}^*$ of the (vectorized) image \mathbf{x} . Theoretical guarantees on the recovery of low-complexity matrices (*e.g.*, sparse, circulant, low-rank) from random ROPs have been extensively studied in the last decade [20–22]. Our sensing model computes SROPs of an *interferometric* matrix built from spatial frequencies of the image. This shares similarities with *random partial Fourier sensing* in CS theory [23,24]. Specifically, the spatial frequencies in this matrix correspond to the difference of the MCF cores locations. This arises in radio-interferometric astronomy applications where, as induced by the van Cittert-Zernike theorem, the signal correlation of two

* E-mail: {o.leblanc, laurent.jacques}@uclouvain.be. ISPGROUP, INMA/ICTEAM, UCLouvain, Louvain-la-Neuve, Belgium. OL is funded by Belgian National Science Foundation (F.R.S.-FNRS).

† Aix Marseille Univ, CNRS, Centrale Méditerranée, Institut Fresnel, Marseille, France. ‡ Cailabs, Rennes, Brittany, France.

antennas gives the Fourier content on a frequency vector (or *visibility*) related to the baseline vector of the antenna pair [13]. One may recognize in [25, Sec. 4.1.] the RS mode described in Sec. II-B. However, in these works, the presence of an interferometric matrix (see *e.g.*, [25, Eq. (15)]) is often implicit, since, conversely to our scheme, no linear combinations of these visibilities are computed.

The 8-step *phase-shifting interferometry* [26] calibration technique (see Sec. V-B) is used in, *e.g.*, astronomical imaging [27], and microscopy [28]). The estimated complex wavefields implicitly encode transmission matrix of the MCF (see [29]) and also embed some unpredictable imperfections in the MCF configuration. Compared to previous work [12] where each speckle generated by a random SLM configuration had to be *a priori* recorded, this calibration is made only once before any acquisition.

B. Contributions

We provide several contributions to the modeling, understanding and efficiency of MCF-LI imaging.

[C1] We incorporate the physics of wave propagation in the sensing model of MCF-LI in Sec. II, showing that it involves applying symmetric rank-one projections, or SROP¹, controlled by the SLM, to an interferometric matrix encoding the spectral content of the image.

[C2] Following the methods of CS theory, we provide recovery guarantees for estimating both the interferometric matrix and the discrete image of the observed object in Secs. III and IV; in particular, we extend previous results from [20] showing that, up to a debiasing, the sensing operator satisfies a variant of the restricted isometry property expressed with an ℓ_1 -norm in the measurement domain, the RIP $_{\ell_2/\ell_1}$. This RIP allows us to prove the optimality of estimating a sparse image with a variant of the basis pursuit denoise program, BPDN $_{\ell_1}$.

[C3] We propose a calibration phase that addresses sensing imperfections in a real setup in Sec. V. This calibration requires a fixed number of observations; it preserves a SROP sensing model and enables the modeling of any further SLM configurations.

Contribution C1 highlights the interferometric behavior of the MCF device, allowing the prediction of speckles in the sample plane \mathcal{Z} based on randomly chosen core complex amplitudes. This moves the previous assumption that the speckle pixels were i.i.d. random coefficients of a projection matrix in [12], to the truly independent random draw of these core complex amplitudes. Contribution C2 utilizes this randomness to prove stable and robust image recovery with high probability under conditions. Provided the components of the SROP complex *sketching* vectors have unit modulus (but random phases), we propose a debiasing trick that does not require doubling the number of measurements (compared to [20])—a definite advantage when recording experimental measurements—but that prevents sensing the sample’s mean. Hopefully, the recovery program BPDN $_{\ell_1}$ recovers that mean for sparse images. Contribution C3 involves a single calibration step that enhances the quality of

speckle prediction from the SLM configuration (reaching 97% of normalized cross-correlation), implicitly registers the cores locations and imaging depth, and corrects system imperfections excepted intercore interferences.

Notations and conventions: Light symbols denote scalars (or scalar functions), and bold symbols refer to vectors and matrices (*e.g.*, $\eta \in \mathbb{R}$, $g \in L_2(\mathbb{R})$, $\mathbf{f} \in \mathbb{R}^N$, $\mathbf{G} \in \mathbb{C}^{N \times N}$). We write $i = \sqrt{-1}$; the identity operator (or $n \times n$ matrix) is Id (resp. Id_n); the set of $Q \times Q$ Hermitian matrices in $\mathbb{C}^{Q \times Q}$ is denoted by \mathcal{H}^Q ; the set of index components is $[M] := \{1, \dots, M\}$; $\{s_q\}_{q=1}^Q$ is the set $\{s_1, \dots, s_Q\}$, and $(a_q)_{q=1}^Q$ the vector $(a_1, \dots, a_Q)^\top$. The notations \cdot^\top , \cdot^* , tr , $\langle \cdot, \cdot \rangle$, correspond to the transpose, conjugate transpose, trace, and inner product. The p -norm (or ℓ_p -norm) is $\|\mathbf{x}\|_p := (\sum_{i=1}^n |x_i|^p)^{1/p}$ for $\mathbf{x} \in \mathbb{C}^n$ and $p \geq 1$, with $\|\cdot\| = \|\cdot\|_2$, and $\|\mathbf{x}\|_\infty := \max_i |x_i|$. Given $\mathbf{A} \in \mathbb{C}^{n \times n}$, $\mathbf{a} \in \mathbb{C}^n$ and $\mathcal{S} \subset [n]$, the matrix $\mathbf{A}_\mathcal{S}$ is made of the columns of \mathbf{A} indexed in \mathcal{S} , the operator $\text{diag}(\mathbf{A}) \in \mathbb{C}^n$ extracts the diagonal of \mathbf{A} , $\text{diag}(\mathbf{a}) \in \mathbb{C}^{n \times n}$ is the diagonal matrix such that $\text{diag}(\mathbf{a})_{ii} = a_i$, $\mathbf{A}_d = \text{diag}(\text{diag}(\mathbf{A}))$ zeros out all off-diagonal entries of \mathbf{A} , and $\|\mathbf{A}\|$ and $\|\mathbf{A}\|_*$ are the operator and nuclear norms of \mathbf{A} , respectively. The direct and inverse continuous Fourier transforms in d dimensions (with $d \in \{1, 2\}$) are defined by $\hat{g}(\boldsymbol{\chi}) := \mathcal{F}[g](\boldsymbol{\chi}) := \int_{\mathbb{R}^d} g(\mathbf{s}) e^{-i2\pi \boldsymbol{\chi}^\top \mathbf{s}} d\mathbf{s}$, with $g : \mathbb{R}^d \rightarrow \mathbb{C}^d$, $\boldsymbol{\chi} \in \mathbb{R}^d$, and $g[\mathbf{s}] = \mathcal{F}^{-1}[\hat{g}](\mathbf{s}) = \int_{\mathbb{R}^d} \hat{g}(\boldsymbol{\chi}) e^{i2\pi \boldsymbol{\chi}^\top \mathbf{s}} d\boldsymbol{\chi}$, with the scalar product $\boldsymbol{\chi}^\top \mathbf{s}$ reducing to ks in one dimension.

II. MCF LENSLESS IMAGING

We here develop the sensing model associated with an MCF lensless imager (MCF-LI). As illustrated in Fig. 1(top), an MCF-LI consists of four main parts: a wavefront shaper (SLM), optics, an MCF and a single photo-detector. The SLM shapes the phase of the light that is injected into the cores. The optics include mirrors and lenses used to focus the light into the center of each core, hence preventing multimodal effects.

As explained below, under a common far-field assumption, MCF-LI can be described as a two-component sensing system applying SROP of a specific interferometric matrix. We show how this model subsumes previous descriptions of the MCF-LI, and end this section highlighting that the SROP and interferometric nature of the model hold beyond the far-field assumptions.

A. Sensing model description

An MCF with diameter D contains Q fiber cores with the same diameter $d < D$ (see Fig. 1(c)). Our goal is to observe an object (or sample) which, for simplicity, is planar and defined in a plane \mathcal{Z} . This plane is parallel to the plane \mathcal{Z}_0 containing the *distal end* of the MCF, and at distance z from it. For convenience, we assume that the origins of \mathcal{Z}_0 and \mathcal{Z} are aligned, *i.e.*, they only differ by a translation in the plane normal direction. In \mathcal{Z}_0 , the Q cores locations are encoded in the set $\Omega := \{\mathbf{p}_q\}_{q=1}^Q \subset \mathbb{R}^2$.

As illustrated in Fig. 1 (and detailed in Sec. V-A and [9]), in MCF-LI the laser light wavefront entering the MCF is shaped with a spatial light modulator (SLM) so that both the light intensity and phase can be individually adjusted for each core at the MCF distal end. Mathematically, assuming a perfectly

¹The ROP terminology was introduced when [21] extended phase retrieval applications [20,30] to the recovery of a low—(but not necessarily one)—rank matrix via rank-one projections.

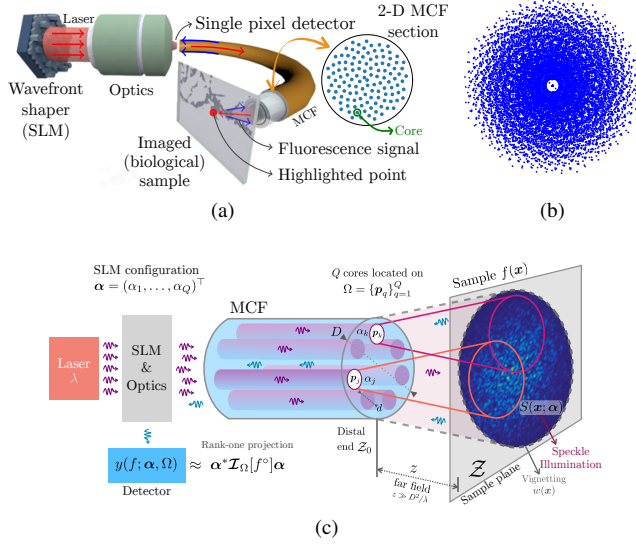


Fig. 1: (a) Working principle of MCF-LI with cores arranged in Fermat's golden spiral when the SLM is programmed in raster scanning mode. (b) Fourier sampling \mathcal{V} corresponding to the core arrangement in (a). (c) Interferometric LI and its link with SRP of the interferometric matrix.

calibrated system, this amounts to setting the Q complex amplitudes $\alpha = (\alpha_1, \dots, \alpha_Q)^T \in \mathbb{C}^Q$, coined *sketching vector*, of the electromagnetic field at each fiber core \mathbf{p}_q with $q \in [Q]$.

Under the far-field approximation, that is if $z \gg D^2/\lambda$ with λ the laser wavelength, the illumination intensity $S(\mathbf{x}; \alpha)$ produced by the MCF on a point $\mathbf{x} \in \mathbb{R}^2$ of the plane \mathcal{Z} reads [12]

$$S(\mathbf{x}; \alpha) \approx w(\mathbf{x}) \left| \sum_{q=1}^Q \alpha_q e^{\frac{i2\pi}{\lambda z} \mathbf{p}_q^T \mathbf{x}} \right|^2, \quad w(\mathbf{x}) := \frac{|\hat{E}_0(\frac{\mathbf{x}}{\lambda z})|}{(\lambda z)^2}. \quad (1)$$

The window $w(\mathbf{x})$, which relates to the output wavefield E_0 of one single core in plane \mathcal{Z}_0 , is a smooth vignetting function defining the imaging field-of-view. Assuming E_0 shaped as a Gaussian kernel of width d , the FOV width scales like $\frac{\lambda z}{d}$.

The sensing model of MCF-LI is established by the following key element: in its endoscope configuration, the sample is observed from the light it re-emits (by fluorescence) from its illumination by S , and for each configuration of S a single pixel detector measures the fraction of that light that propagates backward in the MCF (see Fig. 1(a)). Therefore, given the sample fluorophore density map $f(\mathbf{x})$, assuming a short time exposure and low intensity illumination, fluorescence theory tells us that the number of collected photons $y \in \mathbb{R}_+$ follows a Poisson distribution $\mathcal{P}(\bar{y})$ with average intensity [12]

$$\begin{aligned} \bar{y} &= c \langle S(\cdot, \alpha), f \rangle = c \int_{\mathbb{R}^2} S(\mathbf{x}; \alpha) f(\mathbf{x}) d\mathbf{x} \\ &= c \sum_{j,k=1}^Q \alpha_j^* \alpha_k \int_{\mathbb{R}^2} e^{\frac{i2\pi}{\lambda z} (\mathbf{p}_k - \mathbf{p}_j)^T \mathbf{x}} f^\circ(\mathbf{x}) d\mathbf{x}, \end{aligned} \quad (2)$$

where $0 < c < 1$ represents the fraction of light collected by the pixel detector, and $f^\circ := wf$ is the vignettted image, *i.e.*, the restriction of f to the domain of the vignetting w .

Therefore, assuming $c = 1$ for simplicity, if one collects observations $\mathbf{y} = (y_1, \dots, y_M)^T$, such that $y_m = y(f; \alpha_m, \Omega)$ with distinct vectors α_m ($m \in [M]$), we can compactly write

$$\bar{\mathbf{y}}_m = \alpha_m^* \mathcal{I}_\Omega[f^\circ] \alpha_m = \langle \alpha_m \alpha_m^*, \mathcal{I}_\Omega[f^\circ] \rangle_F, \quad (3)$$

where $\langle \mathbf{A}, \mathbf{B} \rangle_F = \text{tr} \mathbf{A}^* \mathbf{B}$ is the matrix (Frobenius) scalar product between two matrices \mathbf{A} and \mathbf{B} . This amounts to collecting M *sketches* of the Hermitian *interferometric matrix* $\mathcal{I}_\Omega[f^\circ] \in \mathcal{H}^Q$, with entries defined by

$$(\mathcal{I}_\Omega[g])_{jk} := \hat{g}\left[\frac{\mathbf{p}_j - \mathbf{p}_k}{\lambda z}\right] = \int_{\mathbb{R}^2} e^{\frac{i2\pi}{\lambda z} (\mathbf{p}_k - \mathbf{p}_j)^T \mathbf{x}} g(\mathbf{x}) d\mathbf{x}, \quad (4)$$

for any function $g : \mathbb{R}^2 \rightarrow \mathbb{R}$. Under a high photon counting regime, and gathering all possible noise sources in a single additive, zero-mean noise \mathbf{n} , the measurement model reads

$$\mathbf{y} = \mathcal{A} \circ \mathcal{I}_\Omega[f^\circ] + \mathbf{n}, \quad (5)$$

where the *sketching operator* \mathcal{A} defines M SRP [20,21] of any Hermitian matrix \mathbf{H} with

$$\mathcal{A}(\mathbf{H}) := (\langle \alpha_m \alpha_m^*, \mathbf{H} \rangle_F)_{m=1}^M. \quad (6)$$

From (5), MCF-LI corresponds to an *interferometric system* that is linear in f° . Eq. (4) and (6) show that it is indeed tantamount to first sampling the 2-D Fourier transform of f° over frequencies selected in the difference multiset², or *visibilities*,

$$\mathcal{V} := \frac{1}{\lambda z} (\Omega - \Omega) = \{\nu_{jk} := \frac{\mathbf{p}_j - \mathbf{p}_k}{\lambda z}\}_{j,k=1}^Q, \quad (7)$$

i.e., $(\mathcal{I}_\Omega[f^\circ])_{jk} = \mathcal{F}[f^\circ](\nu_{jk})$, and next performing M SRP of $\mathcal{I}_\Omega[f^\circ]$ with the rank-one matrices $\alpha_m \alpha_m^*$ as determined by \mathcal{A} .

Interestingly, the model (5) shows that we cannot access more information about f° than what is encoded in the frequencies of \mathcal{V} . Moreover, this sensing reminds the model of radio-interferometry by aperture synthesis [13]—each fiber core plays somehow the role of a radio telescope and each entry of $(\mathcal{I}_\Omega[f^\circ])_{jk}$ probing the frequency content of f° on the *visibility*³ ν_{jk} .

Assuming we collect enough M SRP observations, we can potentially estimate the interferometric matrix $\mathcal{I}_\Omega[f^\circ]$, which in turn allows us to estimate f° if \mathcal{V} (with $|\mathcal{V}| \leq Q(Q-1)/2$) is dense enough. Actually, the Fermat's golden spiral distribution Ω of the cores depicted in Fig. 1(a)—initially studied for its beam forming performances in MCF-LI by raster scanning [9] (see below)—displays good properties, as shown in Fig. 1(b). For this arrangement, conversely to regular lattice configurations, all (off-diagonal) visibilities are unique, *i.e.*, $|\mathcal{V}| = Q(Q-1)/2$.

B. Connection to known MCF-LI modes

The MCF-LI model subsumes the Raster Scanning (RS) and the speckle illumination (SI) modes introduced in [9,12].

a) Raster scanning mode: In the RS mode, the light wavefront is shaped (or *beamformed*) with the SLM to focus the illumination pattern on the sample plane, while galvanometric mirrors translate the focused beam by phase shifting, hence ensuring the final imaging of the sample by raster scanning the sample and collecting light at each beamed position. A beamformed illumination is equivalent to set $\alpha = \mathbf{1} = (1, \dots, 1)^T$ in (1).

In this case, the illumination intensity S corresponds to

$$S(\mathbf{x}; \mathbf{1}) \approx w(\mathbf{x}) \left| \sum_{q=1}^Q e^{\frac{i2\pi}{\lambda z} \mathbf{p}_q^T \mathbf{x}} \right|^2 = w(\mathbf{x}) |\mathcal{F}[\phi_\Omega(\frac{\mathbf{x}}{\lambda z})]|^2, \quad (8)$$

²The elements of a multiset are not necessarily unique.

³The word “visibility” being actually borrowed from this context.

where ϕ_Ω is the *array factor* of the core arrangement Ω , with, for any finite set $\mathcal{S} \subset \mathbb{R}^2$, $\phi_\mathcal{S}(\mathbf{p}) := \sum_{\mathbf{p}' \in \mathcal{S}} \delta(\mathbf{p} - \mathbf{p}')$. Expanding (8), we also note that $|\mathcal{F}[\phi_\Omega(\frac{\mathbf{x}}{\lambda z})]|^2 = \mathcal{F}[\phi_\mathcal{V}](\mathbf{x})$.

Arranging the core locations as a discretized Fermat's spiral was shown to focus the beam intensity on a narrow spot whose width scales like $\frac{\lambda z}{D}$ [9]. This is induced by the constructive interferences in (8) around $\mathbf{x} \approx \mathbf{0}$ —other locations being associated with almost destructive interferences.

The two galvanometric mirrors adapt the light optical path of the beam according to a tilt vector $\boldsymbol{\theta} \in \mathbb{R}^2$ [12], *i.e.*, $\boldsymbol{\alpha}$ is set to $\boldsymbol{\gamma}_\theta := (\exp(-\frac{i2\pi}{\lambda z} \boldsymbol{\theta}^\top \mathbf{p}_q))_{q=1}^Q$ and (1) provides

$$S(\mathbf{x}; \boldsymbol{\gamma}_\theta) \approx w(\mathbf{x}) \mathcal{T}_\theta \varphi(\mathbf{x}), \quad \mathcal{T}_\theta \varphi(\mathbf{x}) := \varphi(\mathbf{x} - \boldsymbol{\theta}),$$

i.e., $\varphi := \mathcal{F}[\phi_\mathcal{V}](\mathbf{x})$ is translated by $\boldsymbol{\theta}$. We can also write, from the symmetry of φ ,

$$\bar{y}_\theta = \langle S(\cdot, \boldsymbol{\gamma}_\theta), f \rangle = \langle \mathcal{T}_\theta \varphi, f^\circ \rangle = (\varphi * f^\circ)(\boldsymbol{\theta}), \quad (9)$$

with $*$ the 2-D convolution. Therefore, by defining a raster scanning path $\Theta \subset \mathbb{R}^2$ for $\boldsymbol{\theta}$ sequentially visiting all positions in a given 2-D domain within a certain resolution, we see that by collecting all RS observations we image a blurred version (by φ) of f° over Θ . The RS mode is thus characterized by the sketching vectors $\boldsymbol{\alpha} \in \{\boldsymbol{\gamma}_\theta : \boldsymbol{\theta} \in \Theta\}$.

Moreover, by considering the model (3) and the multiset $\mathcal{V}_0 := \{\nu_{jk} : j, k \in [Q], j \neq k\}$ that removes the Q occurrences of the zero frequency from \mathcal{V} , for $\boldsymbol{\theta} = \mathbf{0}$,

$$\bar{y}_0 = \mathbf{1}^\top \mathcal{I}_\Omega[f^\circ] \mathbf{1} = \sum_{\nu \in \mathcal{V}} \hat{f}^\circ[\nu] = Q \hat{f}^\circ[\mathbf{0}] + \sum_{\nu \in \mathcal{V}_0} \hat{f}^\circ[\nu].$$

This shows that \bar{y}_0 probes the content of f° around the origin if the multiset \mathcal{V}_0 is dense enough over the support of \hat{f}° with distinct frequencies; in this case $y_0 - Q \hat{f}^\circ[\mathbf{0}] = \sum_{\nu \in \mathcal{V}_0} \hat{f}^\circ[\nu] \approx c \hat{f}^\circ[\mathbf{0}]$, for some $c > 0$. In this context, the narrowness of the focus relates to the density of \mathcal{V}_0 . Moreover, (3) and (4) provide

$$\bar{y}_\theta = \boldsymbol{\gamma}_\theta^* \mathcal{I}_\Omega[f^\circ] \boldsymbol{\gamma}_\theta = \mathbf{1}^\top \mathcal{I}_\Omega[\mathcal{T}_{-\theta} f^\circ] \mathbf{1}$$

for any tilt $\boldsymbol{\theta}$, meeting the convolution interpretation in (9).

Despite its conceptual simplicity, the RS mode has a few drawbacks [12]: (i) it requires as many illuminations as the target image resolution; (ii) due to limited MCF diameter and the chosen core arrangement, the related convolution kernel φ is actually spatially varying, which limits the validity of (9).

b) Speckle Illumination mode: In the SI mode, the sample f is illuminated with random light patterns called *speckles*. These are generated with random core complex amplitudes $\boldsymbol{\alpha}$. Conversely to the RS mode, by recording all speckles illuminations at calibration, SI does not require to know the MCF transfer matrix.

One can interpret SI as a compressive imaging system [31–33]. By considering that both f and each illumination intensity $S(\mathbf{x}; \boldsymbol{\alpha})$ are discretized and vectorized as $\mathbf{f} \in \mathbb{R}^N$ and $\mathbf{s} \in \mathbb{R}^N$, respectively, and gathering in a matrix $\mathbf{S} := (\mathbf{s}_1, \dots, \mathbf{s}_M) \in \mathbb{R}^{N \times M}$ the M discretized speckles obtained from the sketching vectors $\{\boldsymbol{\alpha}_m\}_{m=1}^M$, the model (5) becomes

$$\bar{y}_m = \mathbf{s}_m^\top \mathbf{f}, \quad m \in [M], \quad \text{or} \quad \bar{\mathbf{y}} = \mathbf{S}^\top \mathbf{f} \in \mathbb{R}_+^M. \quad (10)$$

If M is adjusted to the sparsity level of \mathbf{f} (with $M < N$), the

recovery of \mathbf{f} from $\bar{\mathbf{y}}$ becomes a classical compressive sensing (CS) problem with the sensing matrix \mathbf{S} .

To characterize the properties of the sensing model (10) in this CS framework, the authors in [12] propose to first to center (or *debiase*) this model by computing $\mathbf{y}^c = \bar{\mathbf{y}} - y^a \mathbf{1}_M$ with the measurement average $y^a := \frac{1}{M} \sum_{j=1}^M y_j$ (we reinterpret this operation in Sec. IV-B). This provides, from (10), the model

$$\mathbf{y}^c = \sqrt{M} \boldsymbol{\Phi} \bar{\mathbf{S}} \mathbf{f} + \mathbf{n}^c, \quad (11)$$

with a centered noise $\mathbf{n}^c := \mathbf{n} - (\frac{1}{M} \sum_{j=1}^M n_j) \mathbf{1}_M$, $\sqrt{M} \boldsymbol{\Phi} := \mathbf{D} \mathbf{S}^\top \bar{\mathbf{S}}^{-1}$ and the debiasing matrix $\mathbf{D} := (\mathbf{I}_M - \frac{1}{M} \mathbf{1}_M \mathbf{1}_M^\top)$, $\bar{\mathbf{S}} := \text{diag}(\bar{\mathbf{s}}) \in \mathbb{R}^{N \times N}$, and $\bar{\mathbf{s}} := \mathbb{E}_\alpha \mathbf{s}$. The map $\bar{\mathbf{S}} \mathbf{f}$ relates to the discretization of the vignetted image f° defined above.

The debiasing above allowed the authors of [12] to hypothesize that $\boldsymbol{\Phi}$ satisfies the Restricted Isometry Property (RIP), a crucial property in the classical CS problem [31] ensuring the success of recovery procedures such as the basis pursuit denoise program (see Sec. IV). SI both improves the quality of the reconstructed images and reduces the acquisition time compared to RS. However, the RIP of the related sensing matrix which relies on specific random speckle configurations has not been established, keeping the sample complexity unknown for stable and robust image recovery. Moreover, in SI mode, we must prerecord M —object free—illumination speckles to build $\boldsymbol{\Phi}$, before observing the sample in the imaging plane with the same speckles.

C. Generalized MCF-LI sensing

We can extend the MCF-LI model (3) beyond the far-field and identical core diameter assumptions by replacing the interferometric matrix $\mathcal{I}_\Omega[f^\circ]$ with a more general matrix function $\mathbf{G}[f]$.

Given the wavefield $E_q(\mathbf{x})$ of the q -th core of the MCF in the plane \mathcal{Z} , the illumination reads

$$S(\mathbf{x}; \boldsymbol{\alpha}) := \left| \sum_{q=1}^Q \alpha_q E_q(\mathbf{x}) \right|^2, \quad (12)$$

and similar developments to Sec. II-A provide

$$\bar{y}_m = \boldsymbol{\alpha}_m^* \mathbf{G}[f] \boldsymbol{\alpha}_m = \langle \boldsymbol{\alpha}_m \boldsymbol{\alpha}_m^*, \mathbf{G}[f] \rangle_F \quad (13)$$

where we defined, for any function $h : \mathbb{R}^2 \rightarrow \mathbb{R}$, the Hermitian matrix $\mathbf{G}[h] \in \mathcal{H}^Q$ with entries

$$G_{jk}[h] := \int_{\mathbb{R}^2} E_j^*(\mathbf{x}) E_k(\mathbf{x}) h(\mathbf{x}) d\mathbf{x}. \quad (14)$$

By recording a spatial discretization of the fields $\{E_q(\mathbf{x})\}_{q=1}^Q$, we can thus estimate the forward model (14)—and thus $\mathcal{H}[h] := (\boldsymbol{\alpha}_m^* \mathbf{G}[h] \boldsymbol{\alpha}_m)_{m=1}^M$ —for any function h , as imposed to solve the inverse problem (13) with practical algorithms. While slower than the computation of $\mathcal{I}_\Omega[f^\circ]$ (*e.g.*, with a FFT boosting) and its M SROP, estimating \mathcal{H} directly integrates many deviations to the interferometric model, with a calibration limited to the observation of $\mathcal{O}(Q)$ discretized spatial intensities aimed to yield $\{E_q(\mathbf{x})\}_{q=1}^Q$. We detail in Sec. V-B how to practically achieve this calibration.

III. INTERFEROMETRIC MATRIX RECONSTRUCTION

In the far-field assumption, MCF-LI can thus only access the image frequencies encoded in $\mathcal{I}_\Omega[f^\circ]$, as observed through the sensing model (3). We consider below both deterministic and random SROP constructions to reconstruct the matrix. We show that the minimal number of SROP ensuring reconstruction depends on prior structural assumptions on $\mathcal{I}_\Omega[f^\circ]$.

A. Nyquist reconstruction

We first show that $O(Q^2)$ deterministic sketching vectors suffice to reconstruct any interferometric matrix $\mathcal{I}_\Omega[f^\circ]$ in a noiseless scenario, *i.e.*, a sample complexity upper bound to any further compressive measurements of this matrix.

Proposition 1. *There exists a set of $M = Q(Q-1)+1$ sketching vectors $\{\alpha_m\}_{m=1}^M \in \mathbb{C}^Q$ such that any Hermitian matrix $\mathcal{I} \in \mathcal{H}^Q$ with constant diagonal entries can be reconstructed from the M sketches $y_m = \alpha_m^* \mathcal{I} \alpha_m$.*

Proof. Given the 2-sparse sketching vectors $\alpha_\gamma(q, r) := e_q + \gamma e_r$, with $q, r \in [Q]$, $|\gamma| = 1$ and the s -th canonical vector e_s , we have $h_\gamma[q, r] := \alpha_\gamma^*(q, r) \mathcal{I} \alpha_\gamma(q, r) = \mathcal{I}_{q,q} + \mathcal{I}_{r,r} + \gamma \mathcal{I}_{q,r} + \gamma^* \mathcal{I}_{r,q} = \frac{2}{Q} \text{tr } \mathcal{I} + 2\Re\{\gamma \mathcal{I}_{q,r}\}$. Therefore,

$$h_1[q, r] + i h_{-i}[q, r] = 2\mathcal{I}_{q,r} + \frac{2}{Q}(1+i) \text{tr } \mathcal{I}. \quad (15)$$

From the $Q(Q-1)$ sketching vectors $\{\alpha_\gamma(q, r) : 1 < q < r \leq Q, \gamma \in \{1, -i\}\} \subset \mathbb{C}^Q$, the value $2\Re\{H\} = H + H^*$ computed from the sum $H = \sum_{1 < q < r \leq Q} (h_1[q, r] + i h_{-i}[q, r])$ respects

$$\Re\{H\} = \sum_{q \neq r} \mathcal{I}_{q,r} + (Q-1) \text{tr } \mathcal{I} = \mathbf{1}^\top \mathcal{I} \mathbf{1} + (Q-2) \text{tr } \mathcal{I}.$$

Using the additional unit sketching vector $\mathbf{1}$ thus recovers $\text{tr } \mathcal{I}$ — and all constant diagonal entries of the Hermitian matrix \mathcal{I} — from $\Re\{H\}$, and (15) provides all its off-diagonal entries. Overall \mathcal{I} is thus recovered from $1 + Q(Q-1)$ measurements. \square

B. Compressive reconstruction

Recovering \mathcal{I}_Ω in less than $O(Q^2)$ SROP is possible if this matrix, and thus f , respects specific low-complexity models. First, $\mathcal{I}_0 := \mathcal{I}_\Omega[f^\circ]$ is Hermitian. Moreover, if f° is non-negative, this matrix is positive semi-definite since from (4), for any $\mathbf{v} \in \mathbb{C}^Q$,

$$\begin{aligned} \mathbf{v}^* \mathcal{I}_0 \mathbf{v} &= \int_{\mathbb{R}^2} f^\circ(\mathbf{x}) \sum_{j,k} v_j^* v_k e^{\frac{i2\pi}{\lambda z}(\mathbf{p}_k - \mathbf{p}_j)^\top \mathbf{x}} d\mathbf{x} \\ &= \int_{\mathbb{R}^2} f^\circ(\mathbf{x}) |\mathbf{v}^* \boldsymbol{\rho}(\mathbf{x})|^2 d\mathbf{x} \geq 0, \end{aligned} \quad (16)$$

where $\boldsymbol{\rho} = (\rho_1, \dots, \rho_Q) \in \mathbb{C}^Q$ with $\rho_j(\mathbf{x}) := e^{-\frac{i2\pi}{\lambda z} \mathbf{p}_j^\top \mathbf{x}}$.

Second, if f° is composed of a few Dirac spikes, *i.e.*, if $f^\circ(\mathbf{x}) = \sum_{i=1}^K u_i \delta(\mathbf{x} - \mathbf{x}_i)$ for K coefficients and locations $\{(u_i, \mathbf{x}_i)\}_{i=1}^K$, the interferometric matrix has rank- K since (4) reduces to the sum of K rank-one matrices, *i.e.*,

$$\mathcal{I}_\Omega[f^\circ] = \sum_{i=1}^K u_i \boldsymbol{\rho}(\mathbf{x}_i) \boldsymbol{\rho}^*(\mathbf{x}_i). \quad (17)$$

Under this structural assumption, or if \mathcal{I}_0 is well approximated by a rank- K matrix $(\mathcal{I}_0)_K$, we can recover \mathcal{I}_0 with high probability provided the sketching vectors $\{\alpha_m\}_{m=1}^M$, and thus

\mathcal{A} , are random, *i.e.*, their entries are i.i.d. from a centered sub-Gaussian distribution [20, Thm 1]. In particular, with

$$M \geq M_0 = O(KQ), \quad (18)$$

and probability exceeding $1 - \exp(-cM)$, any matrix \mathcal{I}_0 observed through the model $\mathbf{y} = \mathcal{A}(\mathcal{I}_0) + \boldsymbol{\eta}$, with bounded noise $\|\boldsymbol{\eta}\|_1 \leq \varepsilon$, can be estimated from

$$\tilde{\mathcal{I}} \in \arg \min_{\mathcal{I}} \|\mathcal{I}\|_* \quad \text{s.t.} \quad \mathcal{I} \succcurlyeq 0, \quad \|\mathbf{y} - \mathcal{A}(\mathcal{I})\|_1 \leq \varepsilon.$$

This solution is instance optimal, *i.e.*, for some $C, D > 0$,

$$\|\tilde{\mathcal{I}} - \mathcal{I}_0\|_F \leq C \frac{\|\mathcal{I}_0 - (\mathcal{I}_0)_K\|_*}{\sqrt{K}} + D \frac{\varepsilon}{M}. \quad (19)$$

The sample complexity in (18) is, however, not optimal since for a K -sparse f° , \mathcal{I}_0 depends only on $O(K)$ parameters in (17). While [20] provides similar results with reduced sample complexity provided \mathcal{I}_0 is, *e.g.*, sparse or circulant, these models are not applicable here and we show in Sec. IV that a smaller sample complexity is achievable under certain simplifying assumptions.

IV. IMAGE RECONSTRUCTION

Let us consider a more general compressive sensing framework for MCF-LI directly targeting image estimation within an analysis combining the two sensing components of (3). As proved in Sec. IV-C, from simplifying assumptions made on both f° and the sensing scenario (see Sec. IV-A), this method achieved reduced sample complexities compared to the approach in Sec. III-B, which are also confirmed numerically in Sec. IV-D.

A. Working assumptions

We first assume a bounded field of view in MCF-LI.

Assumption A.1 (Bounded FOV). *The support of the vignetting window $w(\mathbf{x})$ in (1) is contained in a domain $\mathcal{D} := [-L/2, L/2] \times [-L/2, L/2]$ with $L := \frac{c\lambda z}{d}$, for $c > 0$ depending on the (spectrum of the) output wavefield E_0 in (1), and $w = 0$ on the frontier of \mathcal{D} .*

Therefore, supposing f bounded, we have $\text{supp } f^\circ \subset \mathcal{D}$ and $f^\circ = 0$ over the frontier of \mathcal{D} .

We also need to discretize f° by assuming it bandlimited.

Assumption A.2 (Bounded and bandlimited image). *The image f is bounded, and f° is bandlimited with bandlimit $\frac{W}{2}$, with $W := \frac{N_1}{L}$ and $N_1 \in \mathbb{N}$, *i.e.*, $\mathcal{F}[f^\circ](\boldsymbol{\chi}) = 0$ for all $\boldsymbol{\chi}$ with $\|\boldsymbol{\chi}\|_\infty \geq \frac{W}{2}$.*

As will be clear below, this assumption enables the computation of the interferometric matrix $\mathcal{I}_\Omega[f^\circ]$ from the discrete Fourier transform of the following discretization of f° .

From (A.1) and (A.2) the function f° can be identified with a vector $\mathbf{f} \in \mathbb{R}^N$ of $N = N_1^2$ components. Up to a pixel rearrangement, each component f_j of \mathbf{f} is related to one specific pixel of f° taken in the N -point grid

$$\mathcal{G}_N := \frac{L}{N_1} \left\{ (s_1, s_2) \right\}_{s_1, s_2 = -\frac{N_1}{2}^{\frac{N_1}{2}-1}} \subset \mathcal{D}.$$

The discrete Fourier transform (DFT) $\hat{\mathbf{f}}$ of \mathbf{f} is then computed from the 2-D DFT matrix $\mathbf{F} \in \mathbb{C}^{N \times N}$, *i.e.*, $\hat{\mathbf{f}} = \mathbf{F} \mathbf{f} \in$

\mathbb{C}^N , $\mathbf{F} := \mathbf{F}_1 \otimes \mathbf{F}_1$, with $(\mathbf{F}_1)_{kl} = e^{-\frac{i2\pi}{N_1}kl} / \sqrt{N_1}$, $k, l \in [N_1]$, and the Kronecker product \otimes . Each component of $\tilde{\mathbf{f}}$ is related to a 2-D frequency of

$$\hat{\mathcal{G}}_N := \frac{W}{N_1} \{\chi_1, \chi_2\}_{\chi_1, \chi_2 = -\frac{N_1}{2}}^{\frac{N_1}{2}-1} \subset \left[-\frac{W}{2}, \frac{W}{2}\right] \times \left[-\frac{W}{2}, \frac{W}{2}\right].$$

We need now to simplify our selection of the visibilities.

Assumption A.3 (Distinct on-grid non-zero visibilities). *All non-zero visibilities in $\mathcal{V}_0 = \mathcal{V} \setminus \{0\}$ belong to the regular grid $\hat{\mathcal{G}}_N$, i.e., $\mathcal{V}_0 \subset \hat{\mathcal{G}}_N$, and are unique, which means that $|\mathcal{V}_0| = Q(Q-1)$.*

Together, assumptions A.1 and A.2 show that $\mathcal{I}_\Omega[f^\circ]$ can be computed from $\mathbf{F}\mathbf{f}$; for each visibility $\nu_{jk} \in \mathcal{V}$, there is an index $\bar{l} = \bar{l}(j, k) \in [N]$ such that $(\mathcal{I}_\Omega[f^\circ])_{j,k} = \varpi(\mathbf{F}\mathbf{f})_{\bar{l}}$, where $\varpi := \frac{L^2}{\sqrt{N}}$ can be found from the continuous interpolation formula of the Shannon-Nyquist sampling theorem.

Moreover, from A.3, $\bar{l}(j, k)$ is unique for all $j \neq k$ (i.e., $\nu_{j,k} \in \mathcal{V}_0$), and since $(\mathcal{I}_\Omega[f^\circ])_{j,j} = \varpi(\mathbf{F}\mathbf{f})_0$ (i.e., $\bar{l}(j, j) = 0$) for all $j \in [Q]$, we get the equivalence

$$\mathcal{I}_\Omega[f^\circ] = \varpi \mathcal{T}(\mathbf{F}\mathbf{f}), \quad (20)$$

where the operator \mathcal{T} is such that, for all $j, k \in [Q]$ and $\mathbf{u} \in \mathbb{C}^N$, $(\mathcal{T}(\mathbf{u}))_{jk}$ equals u_0 if $j = k$, and $u_{\bar{l}(j,k)}$ otherwise.

Consequently, if f° has zero mean, $(\mathbf{F}\mathbf{f})_0 = 0$ and

$$\frac{1}{\varpi^2} \|\mathcal{I}_\Omega[f^\circ]\|_F^2 = \|\mathbf{R}_{\bar{\mathcal{V}}_0} \mathbf{F}\mathbf{f}\|^2, \quad (21)$$

with $\mathbf{R}_S = \mathbf{Id}_S^\top$ the restriction operator defined for any $S \subset [N]$, and $\bar{\mathcal{V}}_0 = \{\bar{l}(j, k) : j, k \in [Q], j \neq k\} \subset [N]$ the index set of $\mathbf{F}\mathbf{f}$ related to the off-diagonal entries of $\mathcal{I}_\Omega[f^\circ]$ (with $|\mathcal{V}_0| = |\bar{\mathcal{V}}_0|$ from A.3).

As a prior for our image reconstruction procedure, we next suppose that \mathbf{f} is *sparse* in the canonical basis.

Assumption A.4 (Sparsity). *The discrete image \mathbf{f} is K -sparse (in the canonical basis): $\mathbf{f} \in \Sigma_K := \{\mathbf{v} : \|\mathbf{v}\|_0 \leq K\}$.*

While restrictive, our experiments in Sec. V show that other sparsity priors are compatible with our sensing scheme, e.g., the TV norm, postponing to a future work a theoretical justification of such possible extensions.

The next assumption is guided by compressive sensing theory. It ensures that the set of non-zero visibilities \mathcal{V}_0 captures enough information about any sparse image \mathbf{f} .

Assumption A.5 (RIP $_{\ell_2/\ell_2}$ for visibility sampling). *Given a sparsity level K , a distortion $\delta > 0$, and provided*

$$|\mathcal{V}_0| = Q(Q-1) \geq \delta^{-2} K \text{plog}(N, K, \delta), \quad (22)$$

for some polynomials $\text{plog}(N, K, 1/\delta)$ of $\log N$, $\log K$ and $\log 1/\delta$, the matrix $\Phi := \sqrt{N} \mathbf{R}_{\bar{\mathcal{V}}_0} \mathbf{F}$ respects the (ℓ_2/ℓ_2) -restricted isometry, or RIP $_{\ell_2/\ell_2}(\Sigma_K, \delta)$, i.e.,

$$(1 - \delta) \|\mathbf{v}\|^2 \leq \frac{1}{|\mathcal{V}_0|} \|\Phi \mathbf{v}\|_2^2 \leq (1 + \delta) \|\mathbf{v}\|^2, \quad \forall \mathbf{v} \in \Sigma_K.$$

While we do not prove that the visibility set \mathcal{V}_0 defined by the Fermat's spiral core arrangement Ω in MCF-LI verifies A.5, we invoke existing results characterizing compressive sensing with partial Fourier sampling—as established for instance in

the context of tomographic and radio interferometric applications [13, 32]—to prove the existence of a visibility set respecting A.5. For example, from [24, Thm 12.31], if $Q(Q-1) \geq C\delta^{-2}K \log^4(N)$ (for some constant $C > 0$) and the set of $Q(Q-1)$ visibilities $\bar{\mathcal{V}}_0$ are picked uniformly at random in $[N]$, then Φ respects the RIP $_{\ell_2/\ell_2}(\Sigma_K, \delta)$ with probability exceeding $1 - N^{-\log^3 N}$.

We specify now the distribution of the sketching vectors α .

Assumption A.6 (Random sketches with unit modules). *The sketching vectors $\{\alpha_m\}_{m=1}^M$ involved in (5) have components i.i.d. as the random variable $\alpha \in \mathbb{C}$, with $\mathbb{E}\alpha = 0$ and $|\alpha| = 1$.*

The sketching vectors are thus sub-Gaussian, since the sub-Gaussian norm $\|\alpha_q\|_{\psi_2} = \|\alpha_q\|_{\psi_2} = 1$ is bounded (see [34, Sec 5.2.3]). While motivated by the MCF-LI application where the SLM mainly acts on the phase of the core complex amplitudes, this assumption enables a *debiasing trick*, described in Sec. IV-B, which simplifies the theoretical analysis detailed in Sec. IV-C

B. Debaised sensing model

As made clear in Sec. IV-C, the estimation of \mathbf{f} requires a *debiasing* of the MCF-LI measurements imposed by the properties of the SROP operator \mathcal{A} in (3). We follow a debiasing inspired by [12] (and allowed by A.6), with a reduced number of measurements compared to the method proposed in [20].

From (5), we define the *debaised* measurements

$$y_m^c := y_m - \frac{1}{M} \sum_{j=1}^M y_j = \langle \mathbf{A}_m^c, \mathcal{I} \rangle_F + n_m^c, \quad (23)$$

with the centered and the average matrices $\mathbf{A}_m^c = \alpha_m \alpha_m^* - \mathbf{A}^a$ and $\mathbf{A}^a = \frac{1}{M} \sum_{j=1}^M \alpha_j \alpha_j^*$, respectively, $\mathcal{I} := \mathcal{I}_\Omega[f^\circ]$, and noise $n_m^c := n_m - \frac{1}{M} \sum_{j=1}^M n_j$ with $\mathbb{E}|n_m^c|^2 = (1 - \frac{1}{M})\mathbb{E}|n_m|^2$.

Introducing the debaised sensing operator

$$\mathcal{A}^c : \mathcal{J} \in \mathcal{H}^Q \mapsto (\langle \mathbf{A}_m^c, \mathcal{J} \rangle)_{m=1}^M \in \mathbb{R}^M, \quad (24)$$

which respects $\mathcal{A}^c(\mathcal{J}) = \mathcal{A}^c(\mathcal{J}_h)$ with the *hollow* matrix $\mathcal{J}_h := \mathcal{J} - \mathcal{J}_d$ (i.e., $\text{diag}(\mathcal{J}_h) = \mathbf{0}$) since each \mathbf{A}_m^c is hollow from A.6, we can compactly write

$$\mathbf{y}^c = (y_1^c, \dots, y_M^c)^\top = \mathcal{A}^c(\mathcal{I}_h) + \mathbf{n}^c. \quad (25)$$

The debiasing model thus senses, through \mathcal{I}_h , the off-diagonal elements of $\mathcal{I}_\Omega[f^\circ]$. We will show below that the combination of \mathcal{A}^c with the interferometric sensing respects a variant of the RIP property, thus enabling image reconstruction guarantees.

C. Reconstruction analysis

We show now that we can estimate a sparse image \mathbf{f} from its sensing (25). From A.1-A.6, it be recast as

$$\mathbf{y}^c = \mathcal{B}(\mathbf{f}) + \mathbf{n}^c, \quad (26)$$

where, from the equivalence (20), the sensing operator \mathcal{B} reads

$$\mathcal{B} : \mathbf{v} \in \mathbb{R}^N \mapsto \varpi \mathcal{A}^c(\mathcal{T}(\mathbf{F}\mathbf{v})) \in \mathbb{R}_+^M. \quad (27)$$

We propose to estimate \mathbf{f} by solving the basis pursuit denoise program with an ℓ_1 -norm fidelity (or BPDN $_{\ell_1}$), i.e.,

$$\tilde{\mathbf{f}} = \arg \min_{\mathbf{v} \in \mathbb{R}^N} \|\mathbf{v}\|_1 \text{ s.t. } \|\mathbf{y}^c - \mathcal{B}(\mathbf{v})\|_1 \leq \epsilon, \quad (\text{BPDN}_{\ell_1})$$

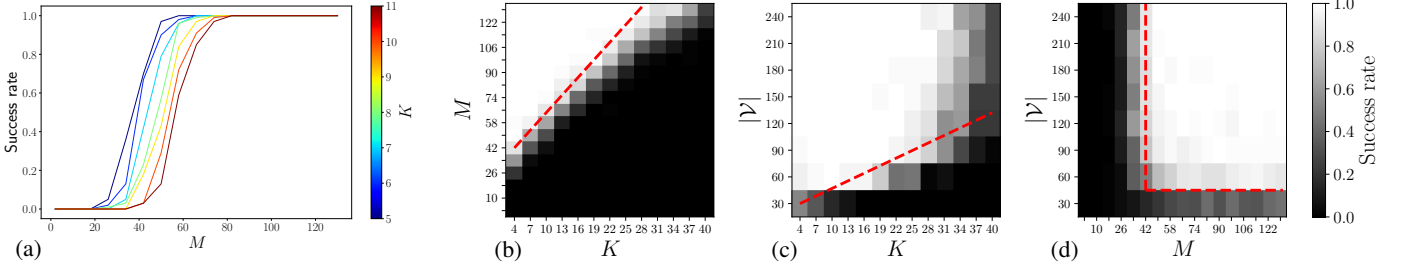


Fig. 2: (a) Transition curves obtained with $|\mathcal{V}| = 240$, ensuring widespread Fourier sampling. The success rate is computed from 100 trials. The transition abscissa shifts to the right for an increasing number K of spikes in \mathbf{f} , indicating more SROP are necessary to reconstruct the interferometric matrix. (b-d) Phase transition diagrams showing M SROP of a $Q \times Q$ interferometric matrix for a K -sparse object \mathbf{f} (with $|\mathcal{V}| = 240$ in (b), $M = 122$ in (c), and $K = 4$ in (d)). One considers a uniformly random 1-D core arrangement and SROP using circularly-symmetric unit-norm random $\{\alpha_m\}_{m=1}^M$. Each pixel is constructed with 80 reconstruction trials solving (34) where we consider success if $\text{SNR} \geq 40\text{dB}$. The probability of success ranges from black (0%) to white (100%). Dashed red lines link the transition frontiers to the samples complexities provided in Sec. IV-A and Sec. IV-C. In (c), the line only coincides with low values of \mathcal{V} due to multiplicity effects.

The specific ℓ_1 -norm fidelity of this program is motivated by the properties of the SROP operator \mathcal{A}^c , and this imposes us to set $\epsilon \geq \|\mathbf{n}^c\|_1$ to reach feasibility. We indeed show below that \mathcal{B} , through its dependence on \mathcal{A}^c , respects a variant of the RIP, the $\text{RIP}_{\ell_2/\ell_1}(\Sigma_K, \mathbf{m}_K, M_K)$: given a sparsity level K , and two constants $0 < \mathbf{m}_K < M_K$, this property imposes

$$\mathbf{m}_K \|\mathbf{v}\| \leq \frac{1}{M} \|\mathcal{B}(\mathbf{v})\|_1 \leq M_K \|\mathbf{v}\|, \quad \forall \mathbf{v} \in \Sigma_K. \quad (28)$$

Under this condition, the error $\|\mathbf{f} - \tilde{\mathbf{f}}\|$ is bounded, *i.e.*, instance optimal [24]. This is shown in the following proposition (inspired by [20, Lemma 2] and proved Appendix A).

Proposition 2 (ℓ_2/ℓ_1 instance optimality of BPDN_{ℓ_1}). *Given K , if there exists an integer $K' > 2K$ such that, for $k \in \{K', K + K'\}$, the operator \mathcal{B} has the $\text{RIP}_{\ell_2/\ell_1}(\Sigma_k, \mathbf{m}_k, M_k)$ for constants $0 < \mathbf{m}_k < M_k < \infty$, and if*

$$\frac{1}{\sqrt{2}} \mathbf{m}_{K+K'} - M_{K'} \frac{\sqrt{K}}{\sqrt{K'}} \geq \gamma > 0, \quad (29)$$

then, for all \mathbf{f} sensed through $\mathbf{y} = \mathcal{B}(\mathbf{f}) + \mathbf{n}^c$ with bounded noise $\|\mathbf{n}^c\|_1 \leq \epsilon$, the estimate $\tilde{\mathbf{f}}$ provided by BPDN_{ℓ_1} satisfies

$$\|\mathbf{f} - \tilde{\mathbf{f}}\| \leq C_0 \frac{\|\mathbf{f} - \mathbf{f}_K\|_1}{\sqrt{K'}} + D_0 \frac{\epsilon}{M}, \quad (30)$$

for two values $C_0 = O(M_{K'}/\gamma)$ and $D_0 = O(1/\gamma)$.

Notice that (29) is satisfied if

$$K' > 8 \left(\frac{M_{K'}}{\mathbf{m}_{K+K'}} \right)^2 K, \quad (31)$$

in which case $\gamma = \frac{1}{2\sqrt{2}} \mathbf{m}_{K+K'}$, and, from App. A, $C_0 = 2(\sqrt{2} + 1)(M_{K'}/\mathbf{m}_{K+K'}) + 2$ and $D_0 = 4(\sqrt{2} + 1)/\mathbf{m}_{K+K'}$.

Interestingly, if both M and $Q(Q-1)$ sufficiently exceed K , the operator \mathcal{B} respects the $\text{RIP}_{\ell_2/\ell_1}$ with high probability.

Proposition 3 ($\text{RIP}_{\ell_2/\ell_1}$ for \mathcal{B}). *Assume that assumptions A.1–A.6 hold, with A.5 set to sparsity level $K_0 > 0$ and distortion $\delta = 1/2$ over the set Σ_{K_0} . For some values $C, c, c_\alpha > 0$ only depending on the distribution of α , if*

$$M \geq CK_0 \ln\left(\frac{12eN}{K_0}\right), \quad Q(Q-1) \geq 4K_0 \log(N, K_0, \delta), \quad (32)$$

then, with probability exceeding $1 - C \exp(-cM)$, the operator \mathcal{B} respects the $\text{RIP}_{\ell_2/\ell_1}(\Sigma_{K_0}, \mathbf{m}_{K_0}, M_{K_0})$ with

$$\mathbf{m}_{K_0} > \frac{\varpi c_\alpha}{3\sqrt{2}} \frac{\sqrt{|\mathcal{V}_0|}}{\sqrt{N}}, \quad \text{and} \quad M_{K_0} < \frac{8\varpi}{3} \frac{\sqrt{|\mathcal{V}_0|}}{\sqrt{N}}. \quad (33)$$

In this proposition, proved in Appendix B, the constants in (33) have not been optimized and may not be tight, *e.g.*, they do not depend on K_0 .

Combining these last two propositions and using the (non-optimal) bounds (33) that are independent of K_0 , since $8(M_{K'}/\mathbf{m}_{K+K'})^2 < \frac{1024}{c_\alpha^2}$, (31) holds if $K' > 1024K/c_\alpha^2$. Therefore, provided \mathcal{B} satisfies the $\text{RIP}_{\ell_2/\ell_1}(\Sigma_{K_0}, \mathbf{m}_{K_0}, M_{K_0})$ for $K_0 \in \{K, K + K'\}$, the instance optimality (30) holds with

$$C_0 < \frac{16(\sqrt{2}+2)}{c_\alpha} = O(1), \quad D_0 = O\left(\frac{\sqrt{N}}{\varpi\sqrt{|\mathcal{V}_0|}}\right) = O\left(\frac{N}{L^2Q}\right).$$

While the constraint on K' imposes a high lower bound on M when the sample complexity (32) is set to $K_0 = (K + K') > (1024/c_\alpha^2 + 1)K$ —as necessary to reach the RIP w.h.p.—the impact of the sparsity error $\|\mathbf{f} - \mathbf{f}_K\|$ in (30) is, however, attenuated by $1/\sqrt{K'} < c_\alpha/(32\sqrt{K})$.

For a fixed FOV L^2 , we also observe a meaningful amplification of the noise error by D_0 when the sampling grid \mathcal{G}_N is too large compared to Q : if the number of pixels N is too small, A.2 may not be verified, since the image bandwidth lower bounds N ; if N is too large the noise error in (30) is vacuous.

D. Phase transition diagrams

We now compare our recovery guarantees with empirical reconstructions obtained on extensive Monte Carlo simulations with S trials and varying parameters K , Q and M .

To save computations, we adopt a simplified setting where (26) is adapted to the sensing of 1-D zero mean sparse vectors in $\mathbb{R}^{N=256}$, without any vignetting, *i.e.*, $f^\circ = f$, and 1-D MCF core locations. At each simulation trial with fixed (K, Q, M) , we verified A.1–A.4 by picking the 1-D cores locations $\{p_q\}_{q=1}^Q \subset \mathbb{R}$ uniformly at random without replacement in $[-\frac{N}{2}, \frac{N}{2}]$, and M sketching vectors $\{\alpha_m\}_{m=1}^M$ i.i.d. as $\alpha \in \mathbb{C}^Q$ with $\alpha_k \sim_{\text{i.i.d.}} e^{i\mathcal{U}([0, 2\pi])}$, $k \in [Q]$. A zero average vector $\mathbf{f} \in \mathbb{R}^{N=256}$ was randomly generated with a K sparse support picked uniformly at random in $[N]$, its K non-zero components obtained with K i.i.d. Gaussian values $\mathcal{N}(0, 1)$ to which we subtracted their average. The interferometric matrix was computed from (20) (with $L = \lambda = z = 1$) using the 1-D FFT matrix \mathbf{F}_1 . We noted that A.3 was only partially verified; at larger Q (and certainly at $Q(Q-1) > N$), non-zero visibilities in the gridded frequency domain $\hat{\mathcal{G}}_N$

can be represented multiple times on low frequencies (*i.e.*, the pdf of the visibilities is essentially triangular if the frequencies are uniform).

To reconstruct \mathbf{f} , we solved the *Lasso* program⁴ [35],

$$\tilde{\mathbf{f}} = \arg \min_{\mathbf{v}} \frac{1}{2} \|\mathbf{y}^c - \mathcal{B}(\mathbf{v})\|^2 \quad \text{s.t.} \quad \|\mathbf{v}\|_1 \leq \tau \quad (34)$$

with $\tau = \|\mathbf{f}\|_1$ set to the actual ℓ_1 -norm of the discrete object. Eq. (34) is equivalent to BPDN $_{\ell_1}$ in a noiseless setting (*i.e.*, $\epsilon = 0$) as it includes an equality constraint $\mathbf{y}^c = \mathcal{B}(\mathbf{f})$ [24, Prop. 3.2]. In the sparse and noiseless sensing scenario set above, we thus expect from (30) in Prop. 2 that $\tilde{\mathbf{f}} = \mathbf{f}$ if \mathcal{B} is RIP $_{\ell_2/\ell_1}$, *i.e.*, if both M and $Q(Q-1)$ sufficiently exceeds K from Prop. 3.

In Fig. 2 and Fig. 2(a), the success rates—*i.e.*, the percentage of trials where the reconstruction SNR exceeded 40 dB—were computed for S set to 80 and 100 trials per value of (K, Q, M) , respectively, and for a range of (K, Q, M) specified in the axes. Since A.3 was partially verified, we tested these rates in function of the averaged value of $|\mathcal{V}| \leq Q(Q-1)$ (which had a std $\leq 0.08N$) over the S trials instead of $Q(Q-1)$. We observe in Fig. 2(b) that high reconstruction success is reached as soon as $M \geq CK$, with $C \simeq 11$, in accordance with (32) in Prop. 3 (up to log factors). Fig. 2(c) highlights that the Fourier sampling $|\mathcal{V}|$ (and thus Q) must increase with K . At small value of Q , we reach high reconstruction success if $|\mathcal{V}| \approx Q(Q-1) \geq C'K$, with $C' \simeq 10$, in agreement with (32) (up to log factors). However, as Q rises that linear trend is biased since the multiplicities in \mathcal{V} increases, *i.e.*, $Q(Q-1) - |\mathcal{V}| \geq 0$ increases. As expected from (32), the transition diagram in Fig. 2(d) shows that at a fixed $K = 4$, both M and $|\mathcal{V}|$ must reach a threshold value to trigger high reconstruction success. In Fig. 2(a), which displays several transition curves of the success rate vs. M for different values of K at $|\mathcal{V}| = 240$, the failure-success transition is shifted towards an increasing number of SROPs when K increases.

V. EXPERIMENTAL MCF-LI

We have tested our approach on proof-of-concept imaging system set in a transmission mode so as to limit both light power loss and Poisson noise [16] on the measurements. We describe below the key aspects of this setup, its specific SLM-to-speckle calibration, before providing examples of reconstructed images.

A. Setup

In the setup explained in Fig. 3, a continuous wave laser operating at $\lambda = 1053\text{nm}$, (YLM-1, IPG Photonics) is expanded and impinges upon a Spatial Light Modulator (SLM X10468-07, Hammamatsu) used to code the incident wavefront to the MCF. The MCF is made of $Q = 110$ cores arranged in Fermat's golden spiral, each exhibiting a single mode at the laser wavelength [12]. The MCF exhibits an inter-core coupling term less than 20 dB [16]. Unlike multimode fibers with stronger core coupling, the focused or speckle patterns generated by an MCF are resilient to thermal and mechanical external perturbations.

The SLM consists of a 800×600 grid of liquid-crystal phase modulators that control the phase of reflected light. As shown

in Fig. 3(a), by mapping specific pixel groups (segments) on the SLM to individual cores of the fiber, an orthogonal basis of input modes is created to modulate the light entering each core. After calibrating the SLM's phase response, any phase pattern in the range of $[0-2\pi]$ can be conveniently represented as an 8-bit grayscale image. The phase pattern on each segment q comprises three terms (*i*) a blazed grating ensures to shift the modulated light to the first-order of the SLM, preventing unmodulated beam from entering the fibers, (*ii*) a convex lens and a series of telescopes produce a focused spot array aligned with the fiber cores, achieving single-modal behavior with a demagnification factor of 64; and (*iii*) a constant phase-offset for each segment which controls the relative phases between the segments.

The light coming from the SLM is focused into the MCF proximal end by Obj₁ ($20 \times / 0.75\text{NA}$, Nikon), then re-expanded on the distal end side with Obj₂ ($20 \times / 0.45\text{NA}$, Olympus). To ensure the validity of the scalar model described in Sec. II-A, a linear polarizer is placed after the fiber end to eliminate any polarization effects. To satisfy the far-field approximation, the object is positioned at the front-focal plane of a lens while the fiber's distal end is placed at the back-focal plane of the same lens [36]. In our setup, the fiber is positioned at the focal plane of Objective lens (Obj₂), and lenses L₁ and L₂ (75 and 100mm, respectively) are used to re-image the conjugate focal plane to a more accessible location on the optical bench (see Fig. 3). The object can be positioned within $\pm 3.5\text{mm}$ tolerance, easily achieved with standard positioning equipment.

The conjugate focal plane is re-imaged onto a 1920×1200 CMOS camera (BFLY-U3-23S6M-C, FLIR) which aids in the calibration and positioning of the system described in Sec. V-B. The same CMOS camera is also used for emulating single-pixel detection by summing up the pixels of the image. Each measurement has an integration time of 19.2ms, and Optical Density (OD) filters are applied to match the light intensity to the camera's dynamic range for improved accuracy. Working in transmission mode, we image a negative 1951 USAF test target mask, contoured in Fig. 3(b). The sample image f is thus binary.

B. Calibration and generalized sensing model

Our MCF-LI setup contains optical system imperfections that are difficult to model. For instance, regarding the hypotheses stated in Sec. II-A, (*i*) the interferometric matrix should be estimated on a set of continuous, off-grid, visibilities, (*ii*) the imaging depth z is a priori unknown and the fiber core diameters are not constant, and (*iii*) the linear polarizer (see Sec. V-A) induces spatially variable, but deterministic, attenuation of the sketching vector component.

Rather than correcting all these deviations one by one, we adopt the generalized MCF-LI sensing introduced in Sec. II-C in (13). This requires us to properly calibrate the system and to determine for each core $q \in [Q]$ the complex wavefields E_q in the object plane \mathcal{Z} from intensity-only measurements. We thus follow a standard 8-step phase-shifting interferometry technique [26]. We first fix a reference core, arbitrarily indexed at $q = 0$, and we program the SLM to activate only that core and another core q , for $1 \leq q \leq Q$. We then record in the

⁴We used SPGL1 [35] (Python module: <https://github.com/drelyea/spgl1>).

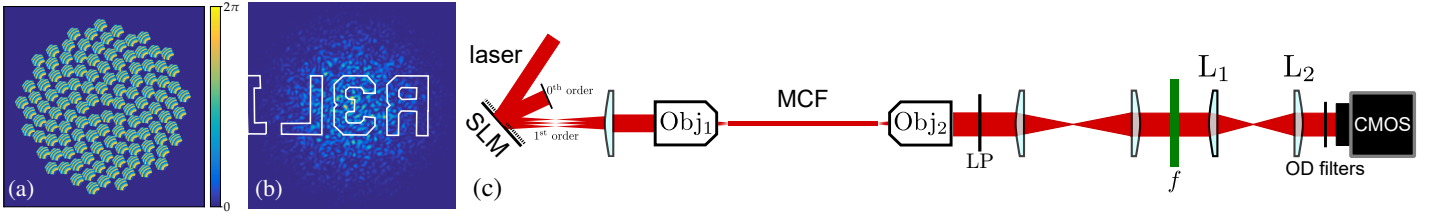


Fig. 3: (a) SLM configuration (800×600 pixels) with lenslet hexagonal arrays dedicated to each core. Blaze gratings applied to each microlens deflect the ray beams towards the MCF proximal end while the 0th beam is reflected out of the optical path. (b) Speckle generated from $\boldsymbol{\alpha} = (e^{i\theta_q})_{q=1}^Q$ with $\theta_q \sim \text{i.i.d. } \mathcal{U}[0, 2\pi]$. The part of the speckle reaching the camera is within the white contour lines representing the studied object f . (c) Schematic of the optical setup. Cutoff $\lambda_c = 600\text{nm}$, SLM=Spatial Light Modulator, MCF=Multi-Core Fiber, LP=Linear Polarizer, f =object to be imaged, OD=Optical Density (neutral density filters).

CMOS camera the 8 fringe patterns $I_{q0}(\mathbf{x}; \phi_k)$ induced by the light interference for 8 different phase steps $\phi_k = \frac{2\pi k}{8}$ ($k \in [8]$) of the reference core, as well as the intensity $I_{00}(\mathbf{x}; 0) = r_0^2(\mathbf{x})$ obtained from activating only the reference core. Mathematically, given the polar representation $r_q(\mathbf{x})e^{i\varphi_q(\mathbf{x})}$ of each complex wavefields,

$$\begin{aligned} I_{q0}(\mathbf{x}; \phi_k) &= |r_0(\mathbf{x})e^{i\varphi_0(\mathbf{x})+\phi_k} + r_q(\mathbf{x})e^{i\varphi_q(\mathbf{x})}|^2 \\ &= I_q^s(\mathbf{x}) + I_q^i(\mathbf{x}) \cos(\varphi_{q0}(\mathbf{x}) + \phi_k), \end{aligned}$$

where $I_q^s := r_0^2 + r_q^2$, $I_q^i := 2r_0r_q$ and $\varphi_{q0} := \varphi_q - \varphi_0$. We can then recover $r_q(\mathbf{x})$ and $\varphi_{q0}(\mathbf{x})$ in each \mathbf{x} by first applying a 8-length DFT on $I_{q0}(\mathbf{x}; \phi_k)$ along the phase steps, and next dividing the last (7-th) DFT coefficient $4I_q^i(\mathbf{x})e^{i\varphi_{q0}(\mathbf{x})}$ by $8r_0(\mathbf{x}) = 8\sqrt{I_{00}(\mathbf{x})}$, which gives

$$\tilde{E}_q(\mathbf{x}) = r_q(\mathbf{x})e^{i(\varphi_q(\mathbf{x})-\varphi_0(\mathbf{x}))} = E_q(\mathbf{x})e^{-i\varphi_0(\mathbf{x})}. \quad (35)$$

From fields estimated in (35) for all $q \in [Q]$, we can reproduce any speckle $S(\mathbf{x}; \boldsymbol{\alpha})$ generated from a sketching vector $\boldsymbol{\alpha} \in \mathbb{C}^Q$ using (12) since this equation is independent of $e^{-i\varphi_0(\mathbf{x})}$.

While the model (13) extends beyond the farfield assumption—it only relies on accurate estimation of the wavefields—the optical constraints followed in Sec. V-A to reach the farfield model are necessary. They allow these fields to not strongly deviate from pure complex exponentials, which preserves the validity of the FOV and sampling assumptions A.1 and A.2 in the sensing model.

In particular, applying the debiasing procedure explained in Sec. IV-B, we get the debiased observation model

$$\mathbf{y}^c = \mathcal{B}(f) + \mathbf{n}^c, \quad (36)$$

where $\mathcal{B}(f)$ is now associated with the generalized interferometric matrix \mathcal{G} defined in (14). In other words, we abuse the notations of (26) and consider a sensing operator $\mathcal{B} : h \mapsto \mathcal{B}(h) := \mathcal{A}^c(\mathcal{G}[h])$ applied to a non-vignetted continuous image h . Regarding the computation of \mathcal{B} , we leverage the calibration to compute an estimate $\hat{\mathcal{B}}(\mathbf{h}) := \mathcal{A}^c(\hat{\mathcal{G}}[\mathbf{h}])$ from a sampling $\mathbf{h} \in \mathbb{R}^{N^2 \simeq N \times N}$ of h , assuming that the proximity to the far-field assumption ensures that $\mathcal{B}(h) \approx \hat{\mathcal{B}}(\mathbf{h})$. For each measurement $m \in [M]$, we in fact compute $z_m = \langle \hat{\mathcal{S}}(\cdot; \boldsymbol{\alpha}_m), \mathbf{h} \rangle$, with $\hat{\mathcal{S}}(\cdot; \boldsymbol{\alpha}_m)$ computed from the estimated fields in (35), before to debias all measurements from (23), i.e., $(\hat{\mathcal{B}}(\mathbf{h}))_m = z_m^c$. Therefore, the matrix $\hat{\mathcal{G}}$ is never explicitly estimated.

C. Results

We now present examples of reconstructed sample images obtained with the considered optical setup described in Sec. V-A, and the calibration and the sensing model from Sec. V-B.

For these experiments, our reconstruction scheme differs from the one followed in Sec. IV. First, as explained in Sec. V-B, the sensing model considers a sampling of the un-vignetted sample image f , with a sensing operator computed in the pixel domain. Second, instead of the ℓ_1 -prior, we decided to estimate this image by promoting a small total variation (TV) norm, as it is more adapted to the cartoon-shape model of the USAF targets. Third, the non-smooth data fidelity term of BPDN_{ℓ_1} is replaced by a smooth square ℓ_2 -norm to ease the iterative computation of the associated convex optimization. We thus solve the following optimization scheme:

$$\tilde{f} = \arg \min_f \frac{1}{2M} \|\mathbf{y}^c - \hat{\mathcal{B}}(f)\|_2^2 + \rho \|f\|_{\text{TV}} \quad \text{s.t. } f \geq 0, \quad (37)$$

with $\rho = O(10^5)$ set empirically. As the vignetting limits the image quality on the frontier of the FOV, we decided to measure the quality of the estimated images with the SNR achieved between the vignetted ground truth $\mathbf{w}f$ and the vignetted reconstruction $\mathbf{w} \odot \tilde{f}$, i.e., $\text{SNR}(\tilde{f}, f) = 20 \log_{10}(\|\mathbf{w} \odot f\|_2 / \|\mathbf{w} \odot (\tilde{f} - f)\|_2)$ with the estimated vignetting $\mathbf{w} := Q^{-1} \sum_{q=1}^Q |\tilde{E}_q|^2$.

Experimental reconstruction analyses are provided in Fig. 4 for images of $N = 256 \times 256$ pixels. In accordance with A.6, the phase of the Q components of the sketch vectors were uniformly drawn i.i.d. in $[0, 2\pi]$ with the 8-bit resolution allowed by the SLM. This configuration maximizes the intensity of light injected in the cores. We tested two values for Q , $Q = 110$, when all the MCF cores are used, and $Q = 55$, by downsampling the Fermat's spiral by a factor 2. In Fig. 4(a), we tested the quality of the reconstruction for $M \in [49, 20\,000]$. Transitions similar to those in Fig. 2(a) occur for a small number of observations and a plateau is reached around $M = 5000$, representing a compression factor of $M/N = 7.6\%$. The highest SNR reached with $Q = 110$ cores is better than with $Q = 55$ cores, as higher image frequencies are captured with the denser core configuration. This effect can also be viewed in Fig. 4(c-d,f-g). Compared to the reconstruction obtained in Fig. 4(e) with the RS mode modeled in Sec. II-B, the TV norm penalty reduces the blur of the reconstructed object. The low SNR values attained in Fig. 4 are due to the comparison of the reconstructed images with an imperfect “ground truth” which is also an estimation of the sample f using white light illumination.

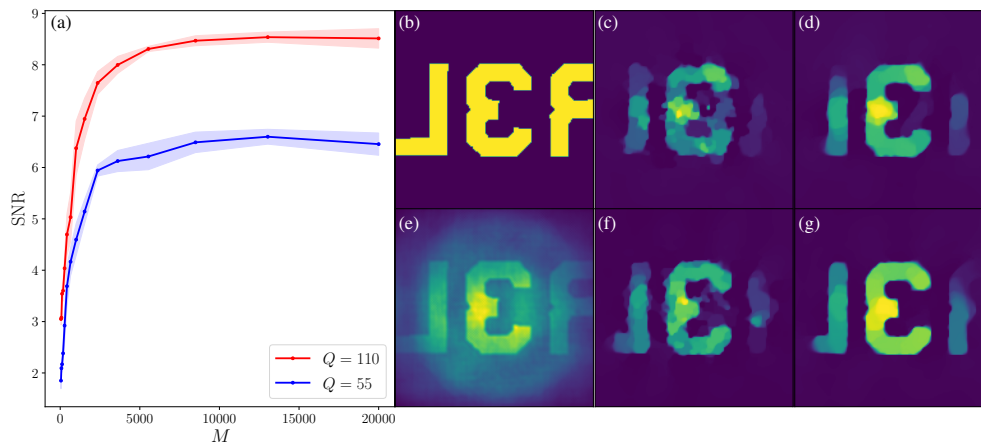


Fig. 4: Experimental reconstruction on $N = 256 \times 256$ images. (a) $\text{SNR}(\mathbf{w}\tilde{\mathbf{f}}, \mathbf{w}\mathbf{f})$ vs. number of observations M for $Q = 55$ (blue) and $Q = 110$ (red) cores. Solid lines represent the average, and light areas show $\pm 1\sigma$ positions from 5 trials. (b) Ground truth \mathbf{f} obtained by illuminating the USAF target with white light passing through the MCF (c-d) Reconstruction using $M = \{49, 2 \cdot 10^4\}$ with $Q = 55$ cores (e) Rec. in RS mode (see Sec. II-B) (f-g) Same as (c-d) with $Q = 110$ cores. (b-g) are zoomed-in versions of the camera plane seen in Fig. 3(b).

VI. CONCLUSION AND PERSPECTIVES

In this paper, we extended the modeling of MCF-LI with speckle illumination by including the physics of light propagation. This new model highlights that the sensing of a 2-D refractive index map of interest is limited both by the number of applied illuminations and the number (and arrangement) of cores at the distal end of the MCF. We provided recovery guarantees and observed the derived sample complexities in both numerical and experimental conditions.

Generalizing our recovery guarantees in Sec. IV to general sparsifying bases $\Psi \neq \text{Id}$ is challenging. In certain bases such as Haar wavelet basis Ψ which includes the constant vector (say on the 1-st column of Ψ), the $\text{RIP}_{\ell_2/\ell_2}$ in (A.5), and thus the $\text{RIP}_{\ell_1/\ell_2}$ of \mathbf{B} in Prop. 3, cannot hold anymore for $\Phi = \sqrt{N}R_{\bar{\nu}_0}\mathbf{F}\Psi$; since $\bar{\nu}_0$ excludes the DC frequency, taking $\mathbf{v} = \lambda\mathbf{e}_1 + \mathbf{e}_k \in \Sigma_2$ with a sufficiently large value λ breaks (A.5). A future research could remove this limitation by particularizing the proofs to sparse signals with zero mean, *i.e.*, belonging to $\Sigma_K^0 := \{\mathbf{v} \in \Sigma_K : \sum_j (\Psi\mathbf{v})_j = 0\}$.

Another limitation of our approach lies in the distinct visibility Assumption A.3. By construction, the density of the visibilities—as achieved by a difference set—cannot be uniform. As shown in Fig. 1(b), this is also true for the golden Fermat’s spiral arrangement. Therefore, when Q grows on a fixed frequency resolution, close visibilities are hardly distinguishable. A more promising sensing model could integrate a variable density sampling (VDS) of the image spectral domain [37,38]. In the same time, this could also allow for more general sparsifying basis by accounting for their variable local coherence with the Fourier basis. However, combining this aspect inside the ROP model is an open question.

Future works about MCF-LI include experimental proof of concept in reflective/endoscopic conditions, extension of the model to vector diffraction theory, and imaging of 3-D maps with generalized ROP models.

ACKNOWLEDGMENT

The authors thank Y. Wiaux for interesting discussions on the link between MCF-LI and radio-interferometry. Computational resources have been provided by the supercomputing facilities of UCLouvain (CISM) and the Consortium des Equipements de Calcul Intensif en Fédération Wallonie Bruxelles (CECI) funded by FRS-FNRS, Belgium. This project has received funding from FRS-FNRS (Learn2Sense, T.0136.20) and European Research Council (ERC, SpeckleCARS, 101052911).

APPENDIX A PROOF OF PROPOSITION 2.

The proof of this proposition is inspired by the one of [20, Lemma 2], itself inspired by [39]. This lemma was developed in the context of sparse matrix recovery from SROP measurements using a variant of BPDN regularized by the trace of the matrix estimate. While certain elements of our proof are similar to the one of that lemma, its adaptation to the context of sparse signal recovery from BPDN_{ℓ_1} (with a ℓ_1 fidelity) is not direct, which justifies the following compact derivations.

Let us first write $\tilde{\mathbf{f}} = \mathbf{f} + \mathbf{h}$ with the true image \mathbf{f} , and some residual $\mathbf{h} \in \mathbb{R}^N$. We define the support $T_0 = \text{supp } \mathbf{f}_K$ containing the indices of the K strongest entries of \mathbf{f} . Next, recursively for $1 \leq i \leq \lceil (N - K)/K' \rceil$, we define the supports $T_i := \text{supp } (\mathbf{h}_{T_i^c})_{K'}$ of length at most K' containing the indices of the K' strongest entries of $\mathbf{h}_{T_i^c}$, with $T_i := \bigcup_{j=0}^{i-1} T_j$, and $T_i^c = [N] \setminus T_i$.

We first observe that, by construction, for all $j \in T_{i+1}$ with $i \geq 1$, $|h_j| \leq \frac{1}{K'} \sum_{l \in T_i} |h_l| = \frac{1}{K'} \|\mathbf{h}_{T_i}\|_1$ so that $\|\mathbf{h}_{T_{i+1}}\|_2^2 \leq \frac{1}{K'} \|\mathbf{h}_{T_i}\|_1^2$. This shows that

$$\sum_{i \geq 2} \|\mathbf{h}_{T_i}\|_1 \leq \frac{1}{\sqrt{K'}} \sum_{i \geq 1} \|\mathbf{h}_{T_i}\|_1 = \frac{1}{\sqrt{K'}} \|\mathbf{h}_{T_0^c}\|_1. \quad (38)$$

By optimality of $\tilde{\mathbf{f}}$ in BPDN_{ℓ_1} and using twice the triangular inequality, we have

$$\begin{aligned} \|\mathbf{f}\|_1 &\geq \|\tilde{\mathbf{f}}\|_1 = \|\mathbf{f} + \mathbf{h}\|_1 \geq \|\mathbf{f}_{T_0} + \mathbf{h}\|_1 - \|\mathbf{f}_{T_0^c}\|_1 \\ &\geq \|\mathbf{f}_{T_0}\|_1 + \|\mathbf{h}_{T_0^c}\|_1 - \|\mathbf{h}_{T_0}\|_1 - \|\mathbf{f}_{T_0^c}\|_1, \end{aligned}$$

so that

$$\|\mathbf{h}_{T_0^c}\|_1 \leq 2\|\mathbf{f}_{T_0^c}\|_1 + \|\mathbf{h}_{T_0}\|_1 \leq 2\|\mathbf{f}_{T_0^c}\|_1 + \sqrt{K}\|\mathbf{h}_{T_0}\|. \quad (39)$$

Therefore, combining (39) and (38) we get

$$\sum_{i \geq 2} \|\mathbf{h}_{T_i}\| \leq 2\frac{\|\mathbf{f}_{T_0^c}\|_1}{\sqrt{K'}} + \frac{\sqrt{K}}{\sqrt{K'}}\|\mathbf{h}_{T_0}\|, \quad (40)$$

By linearity of \mathcal{B} and since both \mathbf{f} and $\tilde{\mathbf{f}}$ are feasible vectors of the BPDN $_{\ell_1}$ constraint, we note that since $\mathbf{h} = \mathbf{f} - \tilde{\mathbf{f}}$

$$\|\mathcal{B}(\mathbf{h})\|_1 \leq \|\mathcal{B}(\mathbf{f}) - \mathbf{y}\|_1 + \|\mathcal{B}(\tilde{\mathbf{f}}) - \mathbf{y}\|_1 \leq 2\epsilon.$$

Therefore, if \mathcal{B} has the RIP $_{\ell_2/\ell_1}(\Sigma_k, m_k, M_k)$ for $k \in \{K', K + K'\}$, we can develop the following inequalities

$$\begin{aligned} \frac{2\epsilon}{M} &\geq \frac{1}{M}\|\mathcal{B}(\mathbf{h})\|_1 \geq \frac{1}{M}\|\mathcal{B}(\mathbf{h}_{T_1})\|_1 - \frac{1}{M}\|\mathcal{B}(\mathbf{h}_{T_1^c})\|_1 \\ &\geq m_{K+K'}\|\mathbf{h}_{T_1}\|_1 - \frac{1}{M}\sum_{i \geq 2} \|\mathcal{B}(\mathbf{h}_{T_i})\|_1 \\ &\geq \frac{1}{\sqrt{2}}m_{K+K'}(\|\mathbf{h}_{T_0}\| + \|\mathbf{h}_{T_1}\|) - \frac{1}{M}\sum_{i \geq 2} \|\mathcal{B}(\mathbf{h}_{T_i})\|_1 \\ &\geq \frac{1}{\sqrt{2}}m_{K+K'}(\|\mathbf{h}_{T_0}\| + \|\mathbf{h}_{T_1}\|) - M_{K'}\sum_{i \geq 2} \|\mathbf{h}_{T_i}\| \\ &\geq \frac{1}{\sqrt{2}}m_{K+K'}(\|\mathbf{h}_{T_0}\| + \|\mathbf{h}_{T_1}\|) - M_{K'}\frac{\|\mathbf{f}_{T_0^c}\|_1 + \sqrt{K}\|\mathbf{h}_{T_0}\|}{\sqrt{K'}}, \end{aligned}$$

where we used several times the triangular inequality, the fact that $|T_i| = K'$ for $i \geq 1$, and (40) in the last inequality. The passage from the second to the third line is due to $\|\mathbf{h}_{T_1}\|_1^2 = \|\mathbf{h}_{T_0}\|_1^2 + \|\mathbf{h}_{T_1}\|_1^2 \geq (\|\mathbf{h}_{T_0}\|_1 + \|\mathbf{h}_{T_1}\|_1)^2/2$.

Therefore, rearranging the terms, and since $\|\mathbf{f}_{T_0^c}\|_1 = \|\mathbf{f} - \mathbf{f}_K\|_1$, we get

$$\begin{aligned} \frac{2\epsilon}{M} + M_{K'}\frac{\|\mathbf{f} - \mathbf{f}_K\|_1}{\sqrt{K'}} &\geq \left(\frac{1}{\sqrt{2}}m_{K+K'} - M_{K'}\frac{\sqrt{K}}{\sqrt{K'}}\right)\|\mathbf{h}_{T_0}\| + \frac{m_{K+K'}}{\sqrt{2}}\|\mathbf{h}_{T_1}\| \\ &\geq \left(\frac{1}{\sqrt{2}}m_{K+K'} - M_{K'}\frac{\sqrt{K}}{\sqrt{K'}}\right)(\|\mathbf{h}_{T_0}\| + \|\mathbf{h}_{T_1}\|). \quad (41) \end{aligned}$$

Finally, if $\frac{1}{\sqrt{2}}m_{K+K'} - M_{K'}\frac{\sqrt{K}}{\sqrt{K'}} \geq \gamma > 0$ and $K' > 2K$, then

$$\begin{aligned} \|\mathbf{f} - \tilde{\mathbf{f}}\| &= \|\mathbf{h}\| \leq \|\mathbf{h}_{T_0}\| + \|\mathbf{h}_{T_1}\| + \sum_{i \geq 2} \|\mathbf{h}_{T_i}\| \\ &\stackrel{(40)}{\leq} \|\mathbf{h}_{T_0}\| + \|\mathbf{h}_{T_1}\| + 2\frac{\|\mathbf{f}_{T_0^c}\|_1}{\sqrt{K'}} + \frac{\sqrt{K}}{\sqrt{K'}}\|\mathbf{h}_{T_0}\| \\ &\leq \frac{\sqrt{2}+1}{\sqrt{2}}(\|\mathbf{h}_{T_0}\| + \|\mathbf{h}_{T_1}\|) + 2\frac{\|\mathbf{f}_{T_0^c}\|_1}{\sqrt{K'}} \\ &\stackrel{(41)}{\leq} \frac{\sqrt{2}+1}{\sqrt{2}}\frac{1}{\gamma}\left(\frac{2\epsilon}{M} + M_{K'}\frac{\|\mathbf{f} - \mathbf{f}_K\|_1}{\sqrt{K'}}\right) + 2\frac{\|\mathbf{f}_{T_0^c}\|_1}{\sqrt{K'}}. \end{aligned}$$

This thus proves the instance optimality (30) by taking

$$C_0 = \frac{\sqrt{2}+1}{\sqrt{2}}\frac{1}{\gamma}M_{K'} + 2, \text{ and } D_0 = 2\frac{\sqrt{2}+1}{\sqrt{2}}\frac{1}{\gamma}.$$

APPENDIX B PROOF OF PROPOSITION 3

We will need the following lemmata to prove Proposition 3. We first need to prove that $\|\mathcal{A}^c(\mathcal{I})\|_1$, with \mathcal{A}^c defined in (24) concentrates around its mean. This slightly extends [20, Prop. 1] where the authors rather proved that the *debaised* operator \mathcal{A}' —such that, for any matrix \mathcal{I} and an even number of measurements $M = 2M'$, $\mathcal{A}'(\mathcal{I})_i := \mathcal{A}(\mathcal{I})_{2i+1} - \mathcal{A}(\mathcal{I})_{2i}$ for $i \in [M']$ —respects the RIP $_{\ell_2/\ell_1}$. This debiasing is introduced to ensure that $\mathbb{E}\mathcal{A}'(\mathcal{I}) = \mathbf{0}$. We show that this is also true for \mathcal{A}^c .

We first show some useful facts about \mathcal{A} and \mathcal{A}^c .

Lemma 4 (Mean and anisotropy of the SROP operator). *Given an Hermitian matrix $\mathcal{I} \in \mathcal{H}^Q$, a zero-mean complex random variable α with $\mathbb{E}\alpha^2 = 0$, and bounded second and fourth moments $\mathbb{E}|\alpha|^2 = \mu_2$, and $\mathbb{E}|\alpha|^4 = \mu_4$, and a set of random vectors $\{\alpha_m\}_{m=1}^M \subset \mathbb{C}^M$ with components i.i.d. as $\alpha_{mq} \sim \alpha$ (for $m \in [M]$, $q \in [Q]$), the SROP operator \mathcal{A} associated with $\{\alpha_m\}_{m=1}^M$ is such that*

$$\mathbb{E}\mathcal{A}_m(\mathcal{I}) = \mathbb{E}\langle \alpha_m \alpha_m^*, \mathcal{I} \rangle = \mu_2 \text{tr} \mathcal{I}, \quad \forall m \in [M] \quad (42)$$

$$\frac{1}{M}\mathbb{E}\mathcal{A}^* \mathcal{A}(\mathcal{I}) = \mu_2^2 \mathcal{I} + (\mu_4 - 2\mu_2^2) \mathcal{I}_d + \mu_2^2(\text{tr} \mathcal{I}) \text{Id}, \quad (43)$$

where the operator \mathcal{A}^* is the adjoint⁵ of \mathcal{A} with

$$\mathcal{A}^* : z \in \mathbb{R}^M \mapsto \mathcal{A}^*(z) := \sum_{m=1}^M z_m \alpha_m \alpha_m^* \in \mathcal{H}^Q,$$

and the matrix $\mathcal{I}_d := \text{diag}(\text{diag}(\mathcal{I}))$ zeroes all but the diagonal entries of \mathcal{I} . Therefore, if $\mathcal{I}, \mathcal{J} \in \mathcal{H}^Q$ with \mathcal{I} hollow, then

$$\mathbb{E}\mathcal{A}^c(\mathcal{J}) = 0, \quad \mathbb{E}\mathcal{A}(\mathcal{I}) = \mathbf{0}, \quad \text{and } \frac{1}{M}\mathbb{E}\mathcal{A}^* \mathcal{A}(\mathcal{I}) = \mu_2^2 \mathcal{I}.$$

Proof. Eq. (42) is an immediate consequence of $\mathbb{E}\alpha_m \alpha_m^* = \mu_2 \text{Id}$. Regarding (43), we first note that $\mathbb{E}\mathcal{A}^* \mathcal{A} \mathcal{I} = \mathbb{E}\sum_{m=1}^M (\alpha_m^* \mathcal{I} \alpha_m) \alpha_m \alpha_m^* = M\mathbb{E}(\alpha^* \mathcal{I} \alpha) \alpha \alpha^*$, and for $q, r \in [Q]$, $[\mathbb{E}(\alpha^* \mathcal{I} \alpha) \alpha \alpha^*]_{qr} = \sum_{j,k=1}^Q \mathcal{I}_{j,k} \mathbb{E}(\alpha_j^* \alpha_k \alpha_q \alpha_r^*)$.

If $q = r$, then $\mathbb{E}(\alpha_j^* \alpha_k \alpha_q \alpha_r^*) = \mathbb{E}(\alpha_j^* \alpha_k |\alpha_q|^2)$ is zero if $j \neq k$, μ_2^2 if $j = k \neq q$, and μ_4 if $j = k = q$. Therefore,

$$\begin{aligned} [\mathbb{E}(\alpha^* \mathcal{I} \alpha) \alpha \alpha^*]_{qq} &= \sum_{j=1}^Q \mathcal{I}_{j,j} \mathbb{E}(|\alpha_j|^2 |\alpha_q|^2) \\ &= \mu_2^2 \text{tr}(\mathcal{I}) + (\mu_4 - \mu_2^2) \mathcal{I}_{qq}. \end{aligned}$$

If $q \neq r$, then $\mathbb{E}(\alpha_j^* \alpha_k \alpha_q \alpha_r^*)$ is non-zero only if $j = q$ and $k = r$ (since $\mathbb{E}\alpha^2 = 0$ and $\mathbb{E}|\alpha|^2 = \mu_2$), in which case it is equal to μ_2^2 . Consequently, $[\mathbb{E}(\alpha^* \mathcal{I} \alpha) \alpha \alpha^*]_{qr} = \mu_2^2 \mathcal{I}_{q,r}$. Gathering these identities, we finally find (43). \square

The next lemma (adapted from [20, App. A]) relates the expectation of $\|\mathcal{A}(\mathcal{I})\|_1$ to the Frobenius norm of hollow matrices \mathcal{I} ; a useful fact for studying below the concentration of $\|\mathcal{A}(\mathcal{I})\|_1$.

Lemma 5 (Controlling the expected SROP ℓ_1 -norm). *In the context of Lemma 4, if the random variable α has unit second moment ($\mu_2 = 1$) and bounded sub-Gaussian norm $\|\alpha\|_{\psi_2} \leq \kappa$ (with $\kappa \geq 1$), then, for any hollow matrix $\mathcal{I} \in \mathcal{H}^Q$, the random variable $\xi := \alpha^* \mathcal{I} \alpha$ is sub-exponential with norm $\|\xi\|_{\psi_1} \leq \kappa^2$, and there exists a value $0 < c_\alpha < 1$, only depending on the distribution of α , such that*

$$c_\alpha \|\mathcal{I}\|_F \leq \frac{1}{M} \mathbb{E}\|\mathcal{A}(\mathcal{I})\|_1 = \mathbb{E}|\xi| \leq \|\mathcal{I}\|_F. \quad (44)$$

Proof. The proof is an easy adaptation of [20, App. A] to the random variable $\xi = \langle \alpha \alpha^*, \mathcal{I} \rangle_F = \alpha^* \mathcal{I} \alpha$, for \mathcal{I} hollow. The constant c_1 (Eq. 50) in that work is here set to 1 since $(\mathbb{E}|\alpha^* \mathcal{I} \alpha|)^2 \leq \mathbb{E}|\alpha^* \mathcal{I} \alpha|^2 = \frac{1}{M} \mathbb{E}\|\mathcal{A}(\mathcal{I})\|_2^2 = \|\mathcal{I}\|_F^2$. \square

The following lemma leverages the result above to characterize the concentration of $\frac{1}{M}\|\mathcal{A}(\mathcal{I})\|_1$.

Lemma 6 (Concentration of SROP in the ℓ_1 -norm). *In the context of Lemmata 4 and 5, given a hollow matrix $\mathcal{I} \in \mathcal{H}^Q$, there exists a value $0 < c_\alpha < 1$, only depending on the*

⁵By definition, the adjoint satisfies $\langle \mathcal{A} \mathbf{M}, \mathbf{v} \rangle_{\mathbb{R}^N} = \langle \mathbf{M}, \mathcal{A}^* \mathbf{v} \rangle_{\mathbb{C}^Q \times \mathbb{C}^Q}$.

distribution of α , such that, for $t \geq 0$, with a failure probability smaller than $2 \exp(-cM \min(t^2, t))$,

$$(c_\alpha - 2t\kappa^2) \|\mathcal{I}\|_F \leq \frac{1}{M} \|\mathcal{A}(\mathcal{I})\|_1 \leq (1 + 2t\kappa^2) \|\mathcal{I}\|_F. \quad (45)$$

Proof. We can assume $\|\mathcal{I}\|_F = 1$ by homogeneity of (45). Defining the random variables $\xi_m := \alpha_m^* \mathcal{I} \alpha_m$ and $\tilde{\xi}_m := |\xi_m| - \mathbb{E}|\xi_m|$ for $m \in [M]$, Lemma 5 shows that each ξ_m is sub-exponential with $\|\xi_m\|_{\psi_1} \leq \kappa^2$. Moreover, using the triangular inequality and $\mathbb{E}|\xi_m| \leq \|\xi_m\|_{\psi_1}$ (from [34, Def. 5.13]), we get $\|\tilde{\xi}_m\|_{\psi_1} \leq \|\xi_m\|_{\psi_1} + \mathbb{E}|\xi_m| \leq 2\kappa^2$, showing the sub-exponentiality of each ξ_m for $m \in [M]$.

Therefore, given $t \geq 0$, using [34, Cor. 5.17], we get, with a failure probability lower than $2 \exp(-cM \min(\frac{t^2}{4\kappa^4}, \frac{t}{2\kappa^2}))$,

$$-t \leq \frac{1}{M} \sum_{m=1}^M \tilde{\xi}_m = \frac{1}{M} \|\mathcal{A}(\mathcal{I})\|_1 - \frac{1}{M} \mathbb{E} \|\mathcal{A}(\mathcal{I})\|_1 \leq t$$

for some $c > 0$. The result follows by applying (44) to lower and upper bound $\frac{1}{M} \mathbb{E} \|\mathcal{A}(\mathcal{I})\|_1$, followed by a rescaling in t . \square

Despite the non-independence of the centered matrices \mathcal{A}_m^c defining the components of \mathcal{A}^c , we can show the concentration of $\mathcal{A}^c(\mathcal{J})$ in the ℓ_1 -norm by noting that, if A.6 holds, $\mathcal{A}_m^c(\mathcal{J}) = \mathcal{A}_m^c(\mathcal{J}_h) = \mathcal{A}_m(\mathcal{J}_h) - \langle \mathbf{A}^a, \mathcal{J}_h \rangle$, applying Lemma 6 on the ℓ_1 -norm of the first term, and noting the second concentrates around 0.

Lemma 7 (Concentration of centered SROP in the ℓ_1 -norm). *In the context of Lemmata 4 and 5 and supposing A.6 holds, given a matrix $\mathcal{J} \in \mathcal{H}^Q$ and $\mathcal{J}_h = \mathcal{J} - \mathcal{J}_d$, there exists a value $0 < c_\alpha < 1$, only depending on the distribution of α , such that, for $t \geq 0$, with a failure probability smaller than $2 \exp(-cM \min(t^2, t))$,*

$$(c_\alpha - 3t\kappa^2) \|\mathcal{J}_h\|_F \leq \frac{1}{M} \|\mathcal{A}^c(\mathcal{J})\|_1 \leq (1 + 3t\kappa^2) \|\mathcal{J}_h\|_F. \quad (46)$$

Proof. Given $\mathcal{J} \in \mathcal{H}^Q$ and its hollow part $\mathcal{J}_h = \mathcal{J} - \mathcal{J}_d$, the operator \mathcal{A}^c is defined componentwise by $\mathcal{A}_m^c(\mathcal{J}) = \mathcal{A}_m(\mathcal{J}) - \langle \mathbf{A}^a, \mathcal{J} \rangle = \langle \alpha_m \alpha_m^* - \mathbf{A}^a, \mathcal{J} \rangle$, with $\mathbf{A}^a = \frac{1}{M} \sum_{j=1}^M \alpha_j \alpha_j^*$. Moreover, from A.6, $\mathcal{A}_m^c(\mathcal{J}) = \mathcal{A}_m^c(\mathcal{J}_h)$ since both matrices $\alpha_m \alpha_m^*$ and \mathbf{A}^a have unit diagonal entries. Therefore, by triangular inequality

$$\left| \frac{1}{M} \|\mathcal{A}^c(\mathcal{J})\|_1 - \frac{1}{M} \|\mathcal{A}(\mathcal{J}_h)\|_1 \right| \leq |\langle \mathbf{A}^a, \mathcal{J}_h \rangle|. \quad (47)$$

Given the i.i.d. random variables $\xi_j = \alpha_j^* \mathcal{J}_h \alpha_j$, we get $\langle \mathbf{A}^a, \mathcal{J}_h \rangle = \frac{1}{M} \sum_{j=1}^M \xi_j$, with $\mathbb{E}\xi_j = 0$ from the hollowness of \mathcal{J}_h . According to Lemma 5, each ξ_j is sub-exponential with $\|\xi_j\|_{\psi_1} \leq \kappa^2$. Therefore, using again [34, Cor. 5.17], we have, with a failure probability lower than $2 \exp(-cM \min(\frac{t^2}{\kappa^4}, \frac{t}{\kappa^2}))$,

$$-t \leq \left\langle \frac{1}{M} \sum_{j=1}^M \alpha_j \alpha_j^*, \mathcal{J}_h \right\rangle \leq t,$$

for some $c > 0$. The result follows from a union bound on the failure of this event and the event (45) in Lemma 6, both inequalities and (47) justifying (46). \square

As a simple corollary of the previous lemma, we can now establish the concentration of $\mathcal{B}(\mathbf{f}) := \varpi \mathcal{A}^c(\mathcal{T}(\mathbf{F}\mathbf{f})) \in \mathbb{R}_+^M$ in the ℓ_1 -norm for an arbitrary K -sparse vector $\mathbf{f} \in \Sigma_K$.

Corollary 1 (Concentration of \mathcal{B} in the ℓ_1 -norm). *In the context of Lemma 7, suppose that A.1- A.6 are respected, with A.5 set*

with sparsity level $K_0 > 0$ and distortion $\delta = 1/2$. Given $\mathbf{f} \in \Sigma_{K_0}$, and the operator \mathcal{B} defined in (27) from the M SROP measurements and the $|\mathcal{V}_0| = Q(Q-1)$ non-zero visibilities with

$$Q(Q-1) \geq 4K_0 \text{plog}(N, K_0, \delta),$$

we have, with a failure probability smaller than $2 \exp(-c'M)$ (for some $c' > 0$ depending only on the distribution of α),

$$\frac{\varpi c_\alpha}{2\sqrt{2}} \frac{\sqrt{|\mathcal{V}_0|}}{\sqrt{N}} \|\mathbf{f}\| \leq \frac{1}{M} \|\mathcal{B}(\mathbf{f})\|_1 \leq 2\varpi \frac{\sqrt{|\mathcal{V}_0|}}{\sqrt{N}} \|\mathbf{f}\|.$$

Proof. Given $\mathbf{f} \in \Sigma_{K_0}$ and $\mathcal{J} = \mathcal{T}(\mathbf{F}\mathbf{f}) \in \mathcal{H}^Q$, let us assume that (46) holds on this matrix with $t = c_\alpha/(6\kappa^2) < 1/6$, an event with probability of failure smaller than $2 \exp(-c'M)$ with $c' > 0$ depending only on c_α and κ , i.e., on the distribution of α . We first note that $\|\mathcal{J}_h\|_F = \|\mathbf{R}_{\mathcal{V}_0} \mathbf{F}\mathbf{f}\|$ from (21). Second,

$$\frac{1}{2} \|\mathbf{f}\|^2 \leq \frac{N}{|\mathcal{V}_0|} \|\mathbf{R}_{\mathcal{V}_0} \mathbf{F}\mathbf{f}\|^2 \leq \frac{3}{2} \|\mathbf{f}\|^2. \quad (48)$$

since from A.5 the matrix $\Phi := \sqrt{N} \mathbf{R}_{\mathcal{V}_0} \mathbf{F}$ respects the $\text{RIP}_{\ell_2/\ell_2}(\Sigma_{K_0}, \delta = 1/2)$ as soon as $|\mathcal{V}_0| = Q(Q-1) \geq 4K_0 \text{plog}(N, K_0, \delta)$. Therefore, since $\mathcal{B}(\mathbf{f}) = \varpi \mathcal{A}^c(\mathcal{J}) = \varpi \mathcal{A}^c(\mathcal{J}_h)$, combining (46) and (48) gives

$$\begin{aligned} \frac{1}{M} \|\mathcal{B}(\mathbf{f})\|_1 &\geq (c_\alpha - 3t\kappa^2) \varpi \|\mathcal{J}_h\|_F \\ &= \frac{1}{2} c_\alpha \varpi \|\mathbf{R}_{\mathcal{V}_0} \mathbf{F}\mathbf{f}\| \geq \frac{\varpi c_\alpha}{2\sqrt{2}} \frac{\sqrt{|\mathcal{V}_0|}}{\sqrt{N}} \|\mathbf{f}\|. \end{aligned}$$

Similarly, using $\sqrt{\frac{3}{2}}(1 + 3t\kappa^2) < (\frac{3}{2})^{3/2} < 2$, we get

$$\frac{1}{M} \|\mathcal{B}(\mathbf{f})\|_1 \leq \sqrt{\frac{3}{2}}(1 + 3t\kappa^2) \varpi \frac{\sqrt{|\mathcal{V}_0|}}{\sqrt{N}} \|\mathbf{f}\| < 2\varpi \frac{\sqrt{|\mathcal{V}_0|}}{\sqrt{N}} \|\mathbf{f}\|. \quad \square$$

We are now ready to prove Proposition 3. We will follow the standard proof strategy developed in [40]. By homogeneity of the $\text{RIP}_{\ell_2/\ell_1}$ in (28), we restrict the proof to unit vectors $\mathbf{f} \in \Sigma_{K_0}$, i.e., $\mathbf{f} \in \Sigma_{K_0}^* := \Sigma_{K_0} \cap \mathbb{S}_2^{N-1}$.

Given a radius $0 < \lambda < 1$, let $\mathcal{G}_\lambda \subset \Sigma_{K_0}^*$ be a λ covering of $\Sigma_{K_0}^*$, i.e., for all $\mathbf{f} \in \Sigma_{K_0}^*$, there exists a $\mathbf{f}' \in \mathcal{G}_\lambda$, with $\text{supp } \mathbf{f}' = \text{supp } \mathbf{f}$, such that $\|\mathbf{f} - \mathbf{f}'\| \leq \lambda$. Such a covering exists and its cardinality is smaller than $\binom{N}{K_0} (1 + \frac{2}{\lambda})^{K_0} \leq (\frac{3eN}{K_0\lambda})^{K_0}$ [40].

Invoking Cor. 1, we can apply the union bound to all points of the covering so that

$$\forall \mathbf{f}' \in \mathcal{G}_\lambda, \quad \frac{\varpi c_\alpha}{2\sqrt{2}} \frac{\sqrt{|\mathcal{V}_0|}}{\sqrt{N}} \leq \frac{1}{M} \|\mathcal{B}(\mathbf{f}')\|_1 \leq 2\varpi \frac{\sqrt{|\mathcal{V}_0|}}{\sqrt{N}}, \quad (49)$$

holds with failure probability smaller than

$$2 \left(\frac{3eN}{K_0\lambda}\right)^{K_0} \exp(-c'M) \leq 2 \exp(K_0 \ln(\frac{3eN}{K_0\lambda}) - c'M).$$

Therefore, there exists a constant $C > 0$ such that, if $M \geq CK_0 \ln(\frac{3eN}{K_0\lambda})$, then (49) holds with probability exceeding $1 - 2 \exp(-c''M)$, for some $c'' > 0$.

Let us assume that this event holds. Then, for any $\mathbf{f} \in \Sigma_{K_0}$,

$$\begin{aligned} \frac{1}{M} \|\mathcal{B}(\mathbf{f})\|_1 &\leq \frac{1}{M} \|\mathcal{B}(\mathbf{f}')\|_1 + \frac{1}{M} \|\mathcal{B}(\mathbf{f} - \mathbf{f}')\|_1 \\ &\leq 2\varpi \frac{\sqrt{|\mathcal{V}_0|}}{\sqrt{N}} + \frac{1}{M} \|\mathcal{B}(\frac{\mathbf{f} - \mathbf{f}'}{\|\mathbf{f} - \mathbf{f}'\|})\|_1 \|\mathbf{f} - \mathbf{f}'\| \\ &\leq 2\varpi \frac{\sqrt{|\mathcal{V}_0|}}{\sqrt{N}} + \frac{1}{M} \|\mathcal{B}(\mathbf{r})\|_1 \lambda, \end{aligned}$$

with the unit vector $\mathbf{r} := \frac{\mathbf{f} - \mathbf{f}'}{\|\mathbf{f} - \mathbf{f}'\|}$. However, this vector \mathbf{r} is itself K_0 -sparse since \mathbf{f} and \mathbf{f}' share the same support. Therefore, applying recursively the same argument on the last term above, and using the fact that $\|\mathcal{B}(\mathbf{w})\|_1$ is bounded for any unit vector \mathbf{w} , we get $\frac{1}{M}\|\mathcal{B}(\mathbf{r})\|_1 \lambda \leq 2\varpi \frac{\sqrt{|\mathcal{V}_0|}}{\sqrt{N}} \sum_{j \geq 1} \lambda^j = 2 \frac{\lambda}{1-\lambda} \varpi \frac{\sqrt{|\mathcal{V}_0|}}{\sqrt{N}}$.

Consequently, since we also have

$$\begin{aligned} \frac{1}{M}\|\mathcal{B}(\mathbf{f})\|_1 &\geq \frac{1}{M}\|\mathcal{B}(\mathbf{f}')\|_1 - \frac{1}{M}\|\mathcal{B}(\mathbf{f} - \mathbf{f}')\|_1 \\ &\geq \frac{\varpi c_\alpha}{2\sqrt{2}} \frac{\sqrt{|\mathcal{V}_0|}}{\sqrt{N}} - \frac{1}{M}\|\mathcal{B}(\mathbf{r})\|_1 \lambda, \end{aligned}$$

we conclude that

$$\frac{\varpi c_\alpha}{2\sqrt{2}} \left(\frac{1-2\lambda}{1-\lambda}\right) \frac{\sqrt{|\mathcal{V}_0|}}{\sqrt{N}} \leq \frac{1}{M}\|\mathcal{B}(\mathbf{f})\|_1 \leq 2\varpi \frac{1}{1-\lambda} \frac{\sqrt{|\mathcal{V}_0|}}{\sqrt{N}},$$

Picking $\lambda = 1/4$ finally shows that, under the conditions described above, \mathcal{B} respects the RIP $_{\ell_2/\ell_1}(\sum K_0, m_{K_0}, M_{K_0})$ with $m_{K_0} > \frac{\varpi c_\alpha}{3\sqrt{2}} \frac{\sqrt{|\mathcal{V}_0|}}{\sqrt{N}}$, and $M_{K_0} < \frac{8\varpi}{3} \frac{\sqrt{|\mathcal{V}_0|}}{\sqrt{N}}$.

REFERENCES

- [1] J. Ables, "Fourier transform photography: a new method for x-ray astronomy," *Publications of the Astronomical Society of Australia*, vol. 1, no. 4, pp. 172–173, 1968.
- [2] R. Dicke, "Scatter-hole cameras for x-rays and gamma rays," *Astrophysical Journal*, vol. 153, p. L101, vol. 153, p. L101, 1968.
- [3] A. Ozcan and E. McLeod, "Lensless imaging and sensing," *Annual Review of Biomedical Engineering*, vol. 18, no. 1, pp. 77–102, 2016, pMID: 27420569.
- [4] G. Kuo, F. L. Liu, I. Grossrubatscher, R. Ng, and L. Waller, "On-chip fluorescence microscopy with a random microlens diffuser," *Opt. Express*, vol. 28, no. 6, pp. 8384–8399, Mar 2020.
- [5] V. Boominathan, J. K. Adams, M. S. Asif, B. W. Avants, J. T. Robinson, R. G. Baraniuk, A. C. Sankaranarayanan, and A. Veeraraghavan, "Lensless Imaging: A computational renaissance," *IEEE Signal Processing Magazine*, vol. 33, no. 5, pp. 23–35, 2016.
- [6] D. Septier, V. Mytskaniuk, R. Habert, D. Labat, K. Baudelle, A. Cassez, G. Brévalle-Wasilewski, M. Conforti, G. Bouwmans, H. Rigneault, and A. Kudlinski, "Label-free highly multimodal nonlinear endoscope," *Opt. Express*, vol. 30, no. 14, pp. 25 020–25 033, Jul 2022.
- [7] B. Lochocki, M. V. Verweg, J. J. M. Hoozemans, J. F. de Boer, and L. V. Amitonova, "Epi-fluorescence imaging of the human brain through a multimode fiber," *APL Photonics*, no. 7, 2022.
- [8] D. Psaltis and C. Moser, "Imaging with Multimode Fibers," *Optics and Photonics News*, vol. 27, no. 1, pp. 24–31, 2016.
- [9] S. Sivankutty, V. Tsvirkun, G. Bouwmans, D. Kogan, D. Oron, E. R. Andresen, and H. Rigneault, "Extended field-of-view in a lensless endoscope using an aperiodic multicore fiber," *Optics Letters*, vol. 41, no. 15, p. 3531, 2016.
- [10] E. R. Andresen, S. Sivankutty, V. Tsvirkun, G. Bouwmans, and H. Rigneault, "Ultrathin endoscopes based on multicore fibers and adaptive optics: status and perspectives," *Journal of Biomedical Optics*, vol. 21, no. 12, p. 121506, 2016.
- [11] W. Choi, M. Kang, and J. e. a. Hong, "Flexible-type ultrathin holographic endoscope for microscopic imaging of unstained biological tissues," *Nature Communications*, vol. 4469, no. 13, 2022.
- [12] S. Guérit, S. Sivankutty, J. Lee, H. Rigneault, and L. Jacques, "Compressive imaging through optical fiber with partial speckle scanning," *SIAM Journal on Imaging Sciences*, vol. 15, no. 2, pp. 387–423, 2022.
- [13] Y. Wiaux, L. Jacques, G. Puy, A. M. Scaife, and P. Vanderghenst, "Compressed sensing imaging techniques for radio interferometry," *Monthly Notices of the Royal Astronomical Society*, vol. 395, no. 3, pp. 1733–1742, 2009.
- [14] M. F. Duarte, M. A. Davenport, D. Takhar, J. N. Laska, T. Sun, K. F. Kelly, and R. G. Baraniuk, "Single-Pixel Imaging via Compressive Sampling," *IEEE Signal Processing Magazine*, vol. 25, no. 2, pp. 83–91, 2008.
- [15] M. Taylor, M. Pashazanoosi, S. Hranilovic, C. Flueraru, A. Orth, and O. Pitts, "Experimental setup for single-pixel imaging of turbulent wavefronts and speckle-based phase retrieval," in *2022 IEEE International Conference on Space Optical Systems and Applications (ICSOS)*, 2022, pp. 78–84.
- [16] S. Sivankutty, V. Tsvirkun, O. Vanvincq, G. Bouwmans, E. R. Andresen, and H. Rigneault, "Nonlinear imaging through a Fermat's golden spiral multicore fiber," *Optics Letters*, vol. 43, no. 15, p. 3638, 2018.
- [17] A. M. Caravaca-Aguirre, S. Singh, S. Labouesse, M. V. Baratta, R. Piestun, and E. Bossy, "Hybrid photoacoustic/fluorescence microendoscopy through a multimode fiber using speckle illumination," pp. 1–10, 2018.
- [18] J. R. Fienup, "Phase retrieval algorithms: a comparison," *Appl. Opt.*, vol. 21, no. 15, pp. 2758–2769, Aug 1982.
- [19] H. H. Bauschke, P. L. Combettes, and D. R. Luke, "Phase retrieval, error reduction algorithm, and fienu variants: a view from convex optimization," *J. Opt. Soc. Am. A*, vol. 19, no. 7, pp. 1334–1345, Jul 2002.
- [20] Y. Chen, Y. Chi, and A. J. Goldsmith, "Exact and stable covariance estimation from quadratic sampling via convex programming," *IEEE Transactions on Information Theory*, vol. 61, no. 7, pp. 4034–4059, 2015.
- [21] T. T. Cai, A. Zhang *et al.*, "Rop: Matrix recovery via rank-one projections," *Annals of Statistics*, vol. 43, no. 1, pp. 102–138, 2015.
- [22] M. Soltani and C. Hegde, "Improved Algorithms for Matrix Recovery from Rank-One Projections," pp. 1–19, 2017.
- [23] E. J. Candès, J. K. Romberg, and T. Tao, "Robust uncertainty principles: Exact signal reconstruction from highly incomplete frequency information," *IEEE Transactions on Information Theory*, vol. 52, no. 2, pp. 489–509, 2006.
- [24] S. Foucart and H. Rauhut, "A mathematical introduction to compressive sensing," *Bull. Am. Math.*, vol. 54, no. 2017, pp. 151–165, 2017.
- [25] A.-J. van der Veen, S. J. Wijnholds, and A. M. Sardarabadi, "Signal processing for radio astronomy," *Handbook of Signal Processing Systems*, pp. 311–360, 2019.
- [26] L. Cai, Q. Liu, and X. Yang, "Simultaneous digital correction of amplitude and phase errors of retrieved wave-front in phase-shifting interferometry with arbitrary phase shift errors," *Optics Communications*, vol. 233, no. 1, pp. 21–26, 2004.
- [27] Rabien, S., Eisenhauer, F., Genzel, R., Davies, R. I., and Ott, T., "Atmospheric turbulence compensation with laser phase shifting interferometry," *A&A*, vol. 450, no. 1, pp. 415–425, 2006.
- [28] P. Mann, V. Singh, S. Tayal, P. Thapa, and D. Mehta, "White light phase shifting interferometric microscopy with whole slide imaging for quantitative analysis of biological samples," *Journal of Biophotonics*, vol. 15, 04 2022.
- [29] S. Sivankutty, V. Tsvirkun, G. Bouwmans, E. R. Andresen, D. Oron, H. Rigneault, and M. A. Alonso, "Single-shot noninterferometric measurement of the phase transmission matrix in multicore fibers," *Opt. Lett.*, vol. 43, no. 18, pp. 4493–4496, Sep 2018.
- [30] E. J. Candès, "PhaseLift : Exact and Stable Signal Recovery from Magnitude Measurements via Convex Programming," 2011.
- [31] E. J. Candès, J. K. Romberg, and T. Tao, "Stable signal recovery from incomplete and inaccurate measurements," *Communications on Pure and Applied Mathematics*, vol. LIX, pp. 1207–1223, 2006.
- [32] E. J. Candès and M. Wakin, "An Introduction To Compressive Sampling," *IEEE Signal Processing Magazine*, vol. 25, no. 2, pp. 21–30, 2008.
- [33] L. Jacques and P. Vanderghenst, "Compressed Sensing: "When sparsity meets sampling,"" in *Optical and Digital Image Processing - Fundamentals and Applications*. Wiley-Blackwell, 2010, pp. 1–30.
- [34] R. Vershynin, "Introduction to the non-asymptotic analysis of random matrices," pp. 210–268, 2010.
- [35] D. E. Van Ewout Berg and M. P. Friedlander, "Probing the pareto frontier for basis pursuit solutions," *SIAM Journal on Scientific Computing*, vol. 31, no. 2, pp. 890–912, 2008.
- [36] J. W. Goodman, *Introduction to Fourier optics*. Roberts and Company Publishers, 2005.
- [37] G. Puy, P. Vanderghenst, and Y. Wiaux, "On variable density compressive sampling," *IEEE Signal Processing Letters*, vol. 18, no. 10, pp. 595–598, 2011.
- [38] B. Adcock, A. C. Hansen, C. Poon, and B. Roman, "Breaking the coherence barrier: A new theory for compressed sensing," *Forum of Mathematics, Sigma*, vol. 5, p. e4, 2017.
- [39] E. J. Candès, "The restricted isometry property and its implications for compressed sensing," *Comptes rendus mathématique*, vol. 346, no. 9-10, pp. 589–592, 2008.
- [40] R. Baraniuk, M. Davenport, R. DeVore, and M. Wakin, "A simple proof of the restricted isometry property for random matrices," *Constructive Approximation*, vol. 28, no. 3, pp. 253–263, 2008.